PS/LPI Note 86-15
May 1986

Report on the Running-In of the electron injection system of LIL-W

J.C. Bourdon, P. Brunet, B. Mouton, E. Plouviez
LAL

S. Battisti, A. Bellanger, R. Bertolotto, D. Blechschmidt,
J.P. Delahaye, B. Frammery, K. Hübner (editor), J.H.B. Madsen,
P. Marti, A. Riche, D.J. Warner
CERN

1. Introduction

This note summarizes the measurements and results obtained during the running-in which took place between December 10th 1985 and January 17th 1986 The layout of the equipment is recalled under point 2 which also describes how the set-up was operated. Measurement of equipment parameters done in the context of the beam tests are given under point 3. The results of the measurements with beam are presented in point 4. Conclusions are presented under point 5.

2. Layout and Mode of Operation

Fig. 1 shows a sketch of the layout. The spectrometer downstream of the converter was temporary and has been removed in the meantime making place for the accelerating section ACS25.

The optics of the beam line gun (GUN 21) to exit of alpha-magnet (BHZ 22) is described in reports by G. Le Meur[1]. These notes are not up-to-date because the distance gun to alpha-magnet had been reduced. The beam behaviour in the line, exit alpha-magnet to exit buncher, has been computed by various authors with increasing quality of approximation by means of PARMELA[2,3,4]. Recently, A. Riche presented preliminary results using a more precise particle tracking[5] but neglecting transverse motion, which is included in PARMELA.

The optics downstream of the buncher was also computed [6]. Appendix I gives the position of all elements in the form of a MAD geometry output and input now including the diaphragm (r = 2.5 mm) at the beam stopper and the vertical steering coils (WDVT251S, WDVT252S) located after the converter and the 45° bending magnet, which were missing in the first MAD version [6].

Since the definitive version of the LIL controls was not available, the equipment was provisionally controlled from three places:

* in klystron gallery (all manual control)
  - RF source: either RF05 (booster klystron) or 500 W source
  - RF station 03: Klystron modulator (MDK03)
    Phasing of prebuncher (PBW22)
    RF signal observation
  - Water cooling
* Control room in EB1 (the NORD driven console could not be used)
  i) Controlled by NODAL programs in three APPLE Macintosh computers[7]
     - RF station 03: attenuation of prebuncher power
     - Magnet power supplies
     - Trigger of MDK05, MDK03, RF gate of 03 (box B), gun W
     - Wire beam scanner WBS25 and SEM grid MSH25.S
  ii) Manual control and observation on scope
     - Gun W
     - Signal from coupling loop in buncher (LBNW)
     - Wall-current monitors (WCM22, WCM25.S)
     - Position and intensity monitors (UMA 22, UMA 25)
* Control in EB1 Equipment Area
     - Vacuum valves, gauges and pumps

The front-end was blocked off from the rest of the linac by two concrete walls (thickness: upstream 80 cm, downstream 40 cm), providing ample protection as measurements by TIS showed. The door to the front-end was interlocked with MDK03 [8].

The main problem for the operation was the inadequate performance of the S-band high-power network which very likely had been polluted already during the RF conditioning by an underrated load of the 7.8 db coupler. Quite some time was wasted until it was realized that the network did not stand more than 11 MW (18 MW nominal) at the input and that nothing could be done about it.

Since the available RF gate plus coupler and isolator (box B) at the klystron input turned out to be rather unreliable, it was decided to use the 500 W source at the beginning of the run in January.

The phase-shifter of the prebuncher could only be manually operated in the klystron gallery, which did not facilitate the operation.

Initially, the insufficient familiarity of the operating crew with the programs and the handling of the NODAL in the APPLE computers caused a significant loss of time.

3. RF Measurements on Prebuncher and Buncher

The buncher measurements were done with a calibrated demodulator (Box C). The attenuation of the cables and of the attenuators was measured. The coupler data were taken from the measurements of SPINNER.

3.1 Prebuncher

The incident power at the prebuncher was measured versus the attenuator setting. The energy gain is given by:

$$\Delta W = \left(2P_i R_s T^2\right)^{\frac{1}{2}} \left(1 - \frac{P_r}{P_i}\right)^{\frac{1}{2}} \left(1 + \left(2Q \frac{\Delta f}{f_0}\right)^2\right)^{-\frac{1}{2}} \qquad (1)$$

where the second term is the reduction factor due to non-zero reflected power and the third term is the drop in real impedance due to the fact that the RF frequency does not agree with the prebuncher eigenfrequency. We get with

T^2R_s = 269 kΩ for β = 0.45 corresponding to 61 keV 9) *)

$1 - (P_r/P_i) = 0.65$ measured

$Q = 9170$ measured 10)

f_0= 2998,854 MHz calculated for T = 27.8°C from
f_0 = 2998.754 MHz at 29,8°C 10)
$\Delta f_0 / \Delta T$ = -50 kHz/°C 10)

f_{RF}= 2998,580 MHz adjusted on 8.1.86 to get best spectrum (before 2998.550 MHz)

$$\Delta W(eV) = 0{,}30 \cdot 10^3 \sqrt{P_i\ (W)} \qquad (2)$$

From SUPERFISH calculations we know

$$E_{z\ max} / \int_0^{\ell} E_z\, dz = 106\ m^{-1} \qquad 9)$$

Taking into account $\Delta W = T \int E_z dz$

$$\text{yields} \quad E_{z\ max}(V/m) = 2.1 \cdot 10^4 \sqrt{P_i(W)} \qquad (3)$$

Fig 2a and 2b give ΔW and $E_{z\ max}$ versus the attenuator setting. The absolute value of the measured power with the cable (4.1 db measured attenuation) as additional attenuation in place turned out to be incorrect. Probably wrong reading of a Philips scope (it has the not very practical feature of indicating two different vertical deflection sensitivities). Since three measurements were made with the same attenuator settings in both series, the absolute value of the power with the cable in could be scaled. If the measurements were without errors, the upper curves would be just a factor 1.6 above the lower curves. Inspection of Fig. 2 shows that the two curves are not simply related by this factor. The levels seem to be correct. PARMELA runs [4] and more recent calculations [5] use $E_{z\ max}$ = 0.5 MV/m. The best spectra were found experimentally with about 2 MV/m (see later).**)

*) This shunt impedance is derived from R_s and Q calculated by SUPERFISH. If the measured Q-value were used, the shunt impedance would only be 3% higher.

**)According to recent measurements by J.C. Bourdon and A. Riche (LPI/Note 86-18), multipactoring starts at $\Delta W < 8$keV or $E_{z\ max} < 0.6$MV/m. Although Fig. 2 indicates that these values are below our working range, multipactoring might have occured at low attenuator settings when the additional attenuation by the cable was used.

3.2 Buncher W

3.2.1 Eigenfrequency versus temperature

In order to determine the correct operating temperature, the minimum reflected power was measured for three temperatures and an incident power of 1MW. Fig. 3 shows the results. Inspection of the curves yields Table I.

Table I, Frequency for P_{rmin} versus temperature reading (MV)

T (°C)	f_{RF} - 2998 MHz (MHz)
27.8	0.62
29	0.48
30.1*	0.45

*Temperature changed during the measurement from 29.3 to 30.9°C.

The least square fit of the data in Table I yields an estimate

$$\Delta f_0/\Delta T = - 75 \text{ kHz/degree}$$

whereas the value expected from LAL-measurements [11] is

$$\Delta f_0/\Delta T = -50 \text{ kHz/degree}$$

If we believe our results the proper temperature setting is 28.5°C for 2998.550 MHz. The difference may be due to the fact that our measurement has been performed with 1MW incident power and without properly waiting for temperature equilibrium. The LAL measurement was done in the limit of vanishing power. However, the derived value 28.5° is not too wrong as comparison with P. Brunet's measurement (25.03.86) shows who found 29° as optimum with 1.4MW incident power. The proper temperature in the limit of zero power is 30.1°C as can be calculated from LAL measurements[11]. It has to be kept in mind that the temperature measurement at CERN is not very precise because the water temperature is not measured at the input and output of buncher W but at input and output of buncher V. The two water circuits are in parallel but quite a distance apart, which could lead to a substantial difference in temperature.

The temperature stability was about ± 0.1°C according to the recordings of F. Hoffmann leading to $< \pm$ 7.5 kHz variation in eigenfrequency. Inspection of Fig. 3 and comparison with the bandwidth $\Delta f = f/2Q =$ 110 kHz according to Q = 13800 [11] shows that this variation is negligible.

3.2.2 Comparison of power measurements

The dissipated power can be determined from the power coupled out from the loop in the buncher, which is known to be 50.3 db below the dissipated power [11]. This power can also be obtained by subtracting the forward from the reflected power at the buncher input. The third, rather rough method is to measure the forward power after the klystron and to take into account the measured attenuation factor (7.41)[12] between klystron 03 and the buncher input. Since the ratio of reflected to incident power at the buncher input was as low as 3.5% in equilibrium, this method should agree with the first two.

Table II, Measured peak power dissipation

Method	P (MW)
Coupling loop (LBNW)	1.2
Input couplers (PBWI, PBWR)	1.1
From klystron output (PKI03)	1.6

It can be seen that the first two measurements agree, whereas the third measurement gives a 40% higher value. It could be that a demodulator box different from the one we think had been used or, more likely, that the attenuation factor of 7.4 between klystron and buncher W was no longer valid since the 7.8 db coupler load had disintegrated and polluted the network.

3.2.3 Energy gain and peak accelerating field

The energy gain for a particle with $\beta = 1$ as function of the dissipated power P is given by

$$\Delta W\ (eV) = T \sqrt{2\ R_s\ \ell\ P} = 3.39 \times 10^3 \sqrt{P\ (W)} \qquad (4)$$

where $T = 0.783$ [11]

$R_s = 27\ M\Omega/m$ [13]

$\ell = 0.35\ m$ [13]

For the comparison with the beam dynamics calculations it is important to know the peak accelerating gradient versus power. This is obtained from

$$\hat{E}_z \text{ (V/m)} = 1.61 \sqrt{(2R_s P)/\ell} = 2.00 \times 10^4 \sqrt{P(W)} \qquad (5)$$

where the numerical factor is derived from the measurements[13]. Note that this is the maximum gradient. The mean of the peak gradients occurring in the invidividual resonating volumes except the $\pi/2$ cells at beginning and end is 95% of this maximum[13].

4. Measurements with Beam

4.1 Momentum

The absolute momentum is obtained from the beam centroid position Δx at the SEM grid MSH 25.S where the calculated dispersion function D_x is -1.28m. Note that we use as all the beam optics codes a right-handed coordinate system. The positive x is to the left of an observer looking down the beam, i.e. in positive z-direction. This convention applied also to the SEM grid readings during these tests. Note also that it was recently decided[14] to adopt the PS instrumentation convention which uses a left-handed system, i.e. the observer has the positive x to his right.

With the calibration constant of the magnet given by LAL[15]

$$p = (- 1.49 \times 10^6)\ I\ (1 - 1.28\ \Delta x) \qquad (6)$$

where I is the current in the magnet.

In order to check this constant, the magnetic field in the magnet was measured with a Hall probe[16]. Since no other calibration magnet could be found, the Hall probe was calibrated with fields $\geq$ 400 G[16]. Using the ratio field over Hall voltage measured at 400 G yields

$$B_y = (- 63.5 \times 10^{-4})\ I$$

Combining this with the magnetic length ℓ_m = 0.6296 m quoted by LAL[15] gives in the current range of interest (-3A > I > -2A)

$$- 1.53 \times 10^6 \left(\frac{eV}{c}/A\right)$$

for the constant in (6). This is 2.5% higher.

It was noticed that the ratio field over Hall voltage dropped by 3% already between 400 and 600 G. Hence, we expect that this ratio is higher at the field of interest (200 G = - 3A) than at 400 G, which leads to an even higher constant in (6) and enhances the discrepancy.

Relying more on the LAL measurements, we shall use the constant in (6) in the rest of the report.

Eight measurements in which the magnet current with a centered spectrum and the buncher loop signal were simultaneously measured are selected for analysis.

The energy gain ΔW_1 is derived from the current measurements using (6) and taking into account the beam energy after the gun (65 keV). The value ΔW_2 is calculated using the measured dissipated power P in (4).

The results are given in Table III in chronological order. The last four measurements form a series where the effective power in the buncher was decreased by moving the gun trigger such that the beam traversed the buncher before the electric field had reached equilibrium. The method was quick but the power could only be determined approximately due to ripple on the loop signal.

Table III, Measured and calculated energy gain in buncher

(I) (A)	p (MeV/c)	ΔW_1 (MeV)	P (MW)	ΔW_2 (MeV)
3.49	5.20	4.65	1.94	4.72
3.12	4.65	4.10	1.04	3.45
3.07	4.57	4.03	1.38	3.99
3.01	4.48	3.93	1.04	3.45
2.87	4.28	3.73	1.00	3.40
2.71	4.04	3.50	0.83	3.09
2.62	3.90	3.36	0.76	2.96

Fig. 4 shows a plot of $(\Delta W)^2$ versus P. The last four values are shown as circles. The straight line corresponds to the expected energy gain ΔW_2 for a given power.

There is a considerable spread amongst the measured points and they do not coincide with the line as they should. It is believed that this mainly reflects the uncertainty in the power measurements with the demodulators.

4.2 Momentum spread

Fig. 5 shows a typical spectrum with the base line shifted to negative values, which occurred very often probably due to stray radiation. Note that the higher energy is to the left, thus the beam is coming towards the observer who is looking upstream. Nearly all the spectra have a steep flank on the high energy side and a longer tail on the low energy side. This characteristic shape was already seen in the spectra of buncher V [17]. The figure captions give the standard derivation $\delta p/p$ and the full width at the base.

A number of simple tests were done: increasing the current in the deflecting magnet moved the spectrum to the right by the correct amount; changing the diaphragm at the converter from the usual Ø 5 mm to 2 mm decreased only the amplitude but not the shape of the spectrum, which also indicated that the beam size at the SEM grid was dominated by the momentum spread as expected [6]; putting in the target instead of the diaphragm made the spectrum disappear altogether; doubling the pulse length of the beam changed only the amplitude by a factor 2 but did not affect the shape of the spectrum.

The expected beam size for $\varepsilon = 4\ \pi$ mm•mrad and for vanishing momentum spread is < 2 mm which corresponds to one bin width.

We attempted to minimize the width of the spectrum by means of the prebuncher. This was hampered by the fact that the amplitude of the spectrum exhibited a periodic, slow variation whose origin was never discovered due to lack of time. The spectrum used to improve suddenly to decrease then slowly and monotonically until the next jump.

Although the time variation and the base line shift cast doubts on the results, the optimum position of the phase shifter and of the attenuator were roughly determined by taking as criterion for the spectrum width the number of bins above the base line. The results are shown in Fig. 8 The position of the phase shifter is given in terms of its position in real space which could not yet been correlated to the actual phase shift between prebuncher and buncher; the scale factor is 7.2 degrees/mm. The intensity at WCM 25.S was about constant (17 mA) over this range of parameters.

Fig. 5 shows one of the optimized spectra. The setting of the phase shifter was rather critical; it had to be set within a few mm, i.e. to about ± 7 degrees. The attenuator had to be set within ± 2 units corresponding to ±5 keV.

In order to examine the energy dependence, the energy was lowered in an other run and the prebuncher parameters optimised using as criterion the spectrum width determined by visual inspection. Fig. 6 gives the initial spectrum and Fig. 7 the spectra at 15% lower energy. There is no drastic change. Whether the widening of the spectrum is really a systematic effect due to the lower energy is difficult to tell.

The three spectra shown in Fig. 7 were recorded within 20 min. The unexplained amplitude variations with time can be clearly seen.

The solenoid SNT25 was varied. No pronounced effect on the spectrum was found proving that the betatron beam size of the beam did not influence the beam width at the SEM grid.

The current in the buncher solenoid SNW23 was changed from the usual value 95A ($\hat{B}$ = 1.1 kG) to 200A ($\hat{B}$ = 2.3 kG) with all other parameters constant. The amplitude of the spectrum was low for higher solenoid currents but the spectrum was well defined up to 190A; it became large at 200A. Whether better steering or different prebuncher parameters would have helped could not be determined due to lack of time.

It is interesting to compare the measured with the calculated spectrum[4] which has a standard deviation of 2.5% and a FW at the base of 9.5%. The mean kinetic energy is 4.22 MeV. Hence, the calculated spectrum is much larger. The difference might be partly due to the fact that the calculated spectrum was obtained with a parameter set chosen for minimum phase spread. Furthermore, the prebuncher had been simulated with a constant field of 0.46 MV/m[9] over 1.5 cm, whereas the field in the experiments was 1.8 MV/m and of Gaussian shape.

More recent simulations [5] with 0.5 MV/m in the prebuncher and a mean kinetic energy of 3.9 MeV indicate a standard deviation of 4.2% at optimum, again larger than the measured one which have a standard deviation of 0.3% and < 3% FW at base (cf. figure captions of Fig. 5, 6 and 7).

6. Current Transmission

The beam pulse length set by the gun was between 20 and 30 ns. Table IV gives a sample of peak current measurements. Not all of them were preceded by an optimization of the focusing and steering.

Table IV, Peak currents (mA)

No	Date	P (GeV/c)	WCM 22	UMA 22	UMA 25	WCM25.S	Comments
1	14.12.	3.41	?	40	36	27	p via P measurement
2	16.12.	?	80	29	22	13	
3	9. 1.	4.6	65	30	30	20	} same settings, second
4	9. 1.	4.6	65	25	22	17	} line 2 hrs. later
5	11. 1.	4.7	59	26	17	15	
6	14. 1.	4.6	69	30	27	22	
7	14. 1.	-	68	34	34	-	Δs (α-magnet)=+5mm, RF off
8	15. 1.	-	68	29	29	-	"
9	15. 1.	?	68	29	11	-	" but RF on
10	15. 1.	?	68	25	21	14 (3.8)	Δs (α-magnet)=+9mm, RF on
11	17. 1.	4.6	150	18	17	10	Δs (α-magnet)=+5mm, RF on

All the current measurements at WCM25.S were done with the 5 mm diameter diaphragm at the converter which is responsible for the intensity reduction between UMA24 and WCM25.S. Using the 2 mm diameter diaphragm further reduces the current. The value in the parenthesis in case 10 gives the reduced current as example. Obviously, this reduction critically depends on the centering of the beam at the converter.

The α-magnet was displaced in case 7 to 10 in the direction of the beam coming from the gun in order to study the influence of its position on the transmission, which turned out to be rather insensitive to the α-magnet position.

Comparison of case 8 and 9 shows the reduction of the transmission through the buncher due to the RF fields. According to the logbook, the attenuator was at 470, i.e. hardly any attenuation, implying an energy gain of about 130 keV in the prebuncher. Although this energy gain exceeds the gun voltage, the electrons were not reflected at the prebuncher. Otherwise the current at UMA22 would have been lower with RF on. The particles are reflected at the buncher and get lost. This behaviour was also seen during the LIL front-end V tests at Orsay[17] and it is in agreement with the computations[18]. Although a similar detailed analysis of the bunching system W is still missing, the general beam behaviour will certainly be the same as in the bunching system V.

The nominal resolved electron current is 40 mA at 600 MeV. Assuming about 90% transmission through the eventually well-tuned linac implies that ≈ 45 mA are required after the diaphragm at the converter. For operation with some margin 60 mA would be welcome. Table IV indicates that about 1/3 of the desired current was obtained.

Table V gives the current transmission from one monitor to the next. The first line gives the transmission averaged over the first 6 cases of Table IV. The second line is an average over line 7 and 8.

Table V, Beam transmission

Case	UMA22/WCM22	UMA25/UMA22	WCM25.S/UMA25	Comment
<1...6>	0.42	0.85	0.75	-
<7,8>	0.46	1.0	-	$\Delta S(\alpha)$ = + 5 mm, RF off
9	0.43	0.38	-	$\Delta S(\alpha)$ = + 5 mm, RF on
10	0.37	0.84	0.67 (0.18)	$\Delta S(\alpha)$ = + 9 mm, RF on
11	0.12	0.94	0.59	$\Delta S(\alpha)$ = + 5 mm, RF on

The drop in transmission between WCM22 and UMA22, case 10 and 11, is obvious. It was also noted that a drastic reduction in vertical steering (DVT221) together with an increase in gun current was required to get the beam intensity from 3 mA back to about 20 mA at UMA22. The usual, but abnormally high value of 0.7 A in DVT221, providing a deflection of about 0.11 rad (sic), had to be reduced to 0.03A (deflection 5mrad). The reason became apparent in March 1986, when the gun had to be repaired and a change in gun geometry was discovered.

Fig. 9 shows the current after the buncher at UMA22 with constant input current from the gun (150 mA) versus phase with the attenuator setting as parameter. It can be seen that an optimum prebuncher setting increases the current by 50% compared to prebuncher off (disconnected). However, a wrong setting reduces it to 50%.

Note that the transmission factor through the buncher is not known because the current at UMA22, which can be strongly influenced by reflected electrons at higher field levels in the prebuncher, was not measured simultaneously.

Fig. 11 shows the maximum current at UMA25 for a given attenuator setting expressed in terms of energy gain (cf. Fig. 2). The optimum phase setting found at the maxima of Fig. 9 is also shown. The density of points is insufficient to determine with certainty the functional dependence. The dashed line is a guess.

Fig. 10 shows the attenuator setting for maximum current at WCM25.S versus phase shifter position.

It is interesting to note that the current transmitted is monotonically increasing with the energy gain in the prebuncher. Whether also the bunching factor (current in a given phase interval/total transmitted current) is concurrently enhanced is not known.

A correlation with the energy spectrum was not possible during these transmission measurements.

A 100 μm AL sheet had been introduced in the last run in front of the foils forming the SEM grid in order to suppress the base line shift suspected to be due to low energy stray electrons coming along with the beam. The distance between AL sheet and foils was 20 cm. Unfortunately, this made the signal disappear completely. Radiation and secondary electrons from the foil might be the reason.

The vertical steering coils DVT251.S and DVT252.S were used, but it did not help to find the spectrum.

7. Emittance Estimate

The beam size just before the converter diaphragm was measured with the wire beam scanner (WBS25). Fig. 12 shows the beam size at two different energies versus the current in the lens (SNT25) focusing the beam at the diaphragm. It can be seen that the beam can be focused to a diameter close to the diameter of the diaphragm (5 mm). The energy dependence could not be resolved. The vertical beam size with small solenoid (SNT25) currents is not very reliable because of the bad signal to noise ratio.

Fig. 13 is a similar diagram but with the current in the buncher solenoid as parameter. The magnetic field was 0.82, 1.1 and 1.6 kG corresponding to the currents 70, 95 and 140A. The two sets of values at 70A

refer to two sets of steering before the buncher. The horizontal beam width is influenced; the vertical beam size is hardly affected. The usual value of 95A seems to give the smallest beam but it could also be that the steering was better for this value because it had received more attention.

An estimate of the three beam parameters (α, β, ε) can be obtained using the following arguments. For symmetry reasons the ellipses are expected to be erect in the two phase planes at the buncher exit, i.e. $\alpha_i = 0$. Since the beam is fairly round, it is sufficient to consider one plane. As the rotation of the phase planes by SNT25 is irrelevant for the following considerations, it is neglected. The thin lens approximation is used for the quadrupole model of the solenoid having a focal length of 0.41m at 100A and at 4 MeV kinetic energy.

Having this model the β-values at WBS25 β_W can be calculated as function of the solenoid current and of the beta value β_i at buncher exit. Using as most reliable point the beam width with 100A in SNT25, which always was 5 mm for I(SNW23) = 95 A, the emittance can be calculated. Table VI shows the results.

The additional information contained in the dependence of beam size on SNT25 current turns out to be of little use for choosing the probable β_i, because this dependence is hardly influenced by the β_i as the last two columns of Table VI show which give the relative increase in beam size for two, lower solenoid currents. Hence it seems that these data only provide an upper limit $\varepsilon \leq 12\ \pi$ mm.mrad. The acceptance of the buncher is $240\ \pi$ mm.mrad.

Table VI, β_W(at WBS25) and emittance versus initial β

β_i m	β_W (100A) m	ε/π mm.mrad	$\left(\frac{\beta_W\ (0A)}{\beta_W\ (100A)}\right)^{\frac{1}{2}}$	$\left(\frac{\beta_W\ (50A)}{\beta_W\ (100A)}\right)^{\frac{1}{2}}$
1/16	2.25	1.24	1.77	1.39
1/4	1.14	4.8	1.80	1.40
1	0.71	12.4	1.93	1.49
4	0.91	7.5	2.26	1.63
16	1.74	2.1	2.30	1.65

Fig. 14 shows the current passing the diaphragm recorded simultaneously with the data of Fig. 13. Here again the superiority of 95A in SNW23 is apparent which probably profited from a better steering of the beam at the diaphragm. It appears that most of the incident current passed in this case.

Fig. 15 shows the transmitted current versus the ratio of diaphragm to beam radius taken from Fig. 13. The expected behavior of a Gaussian beam is also plotted. The beam current with I = 70 A in SNW23 was probably low because the beam was not correctly centered.

Projecting the aperture limitation by the diaphragm onto the phase space at the booster exit for the different solenoid SNT25 settings yields Fig. 16. All particles between the lines g_1 and g_2 at the buncher exit will pass the diaphragm.

Consider the current at WCM25.S in the 95A (SNW23) case (Fig. 14). Inspection of Fig. 15 suggests that this monotonic current increase by a factor 2 with close saturation at I(SNT25) = 100 A is only possible if the beam is about 1 mm x 4mrad at the buncher exit (α_i = 0 assumed). This would imply $\beta_i \approx 0.25$ m and a beam diameter of 4.6 mm at the diaphragm for I(SNT25) = 100 A, which is not incompatible with the data of Fig. 12 and 13.

The expected variation with current of SNT25 is shown in Fig. 12 by a dashed line. Although horizontally the agreement with the data is not so bad, vertically the fit fails at small solenoid currents, but there the data are unreliable because the measurement of the signal was often difficult due to low signal levels.

Hence, the emittance is somewhere between 4 and 12 π mm.mrad at p = 4.5 MeV/c leading to $\varepsilon\beta\gamma$ = 36 to 110 $\pi \cdot 10^{-6}$ m.rad, which is smaller by > 50 than the expected linac admittance for positrons. The design value for the invariant emittance was $< 80\ \pi\ 10^{-6}$ m.rad.

Table VII gives the brilliance defined as

$$B = I/(\varepsilon\beta\gamma/\pi)^2$$

for the beam provided by LIL buncher W and buncher V [19]. For comparison the brilliance of the SLC injector[20] is given. The current of 24A corresponds to 5.10^{10} electrons/bunch.

Table VII, Comparison of Brilliance B

Front-end	Kinetic Energy MeV	Current A	$\varepsilon\beta\gamma/\pi$ mrad.m	B A/m^2
W	4	$\leq$ 0.036	0.04 - 0.1	3 - 23
V	25	$\leq$ 8	0.5 - 0.6	22 - 32
SLC	40	$\leq$ 24	0.4	150

Since the emittance is probably closer to the lower than to the upper limit, it can be concluded that front-end W has a brightness similar to front-end V. The SLC brightness is clearly superior.

8. Conclusions

The measured performance of the front-end is very close to the expected one. The energy of the beam (4 MeV) agrees well with the energy gain calculated from the input power. The energy spread ($\leq$ 3% FW at the base) is even smaller than expected.

The current is somewhat limited ($\leq$ 35 mA after the buncher). About three times more would be preferred. The emittance could only indirectly be estimated to be between $0.04 \times 10^{-3} \leq \varepsilon\beta\gamma \leq 0.1 \times 10^{-3}$ rad.m. The brilliance is comparable to the brilliance of the front-end V.

Many LPI components and systems could be tested for the first time during these runs. All of them functioned very well after some tuning except the high-power network which limited the power to about 11 MW very early in the runs because it had become polluted by the decomposition of an underrated RF load at a coupler.

9. Acknowledgements

This sucessful beam test would have been impossible without the effort of LAL/PI and of the whole LPI group. We are also very grateful for the substantial help from all the other PS groups. D.J. Warner and J.C. Bourdon critically read the manuscript and made numerous useful suggestions.

POS. NO.	ELEMENT NAME	OCC. NO.	SEQUENCE SUM(L) [M]	SEQUENCE ARC [M]	I I	POSITIONS X [M]	POSITIONS Y [M]	POSITIONS Z [M]	I I	ANGLES THETA [RAD]	ANGLES PHI [RAD]	ANGLES PSI [RAD]
BEGIN	BLGWIL	1	0.0	0.0		0.0	0.0	0.0		0.0	0.0	0.0
BEGIN	BLL21	1	0.0	0.0		0.0	0.0	0.0		0.0	0.0	0.0
1	WGUN210	1	0.055000	0.055000		0.0	0.0	0.055000		0.0	0.0	0.0
2	WDRI211	1	0.096400	0.096400		0.0	0.0	0.096400		0.0	0.0	0.0
3	WDVT221U	1	0.116400	0.116400		0.0	0.0	0.116400		0.0	0.0	0.0
4	WDVT221D	1	0.136400	0.136400		0.0	0.0	0.136400		0.0	0.0	0.0
5	WDRI212	1	0.259000	0.259000		0.0	0.0	0.259000		0.0	0.0	0.0
END	BLL21	1	0.259000	0.259000		0.0	0.0	0.259000		0.0	0.0	0.0
BEGIN	BLL22U	1	0.259000	0.259000		0.0	0.0	0.259000		0.0	0.0	0.0
6	WDRI221	1	0.266500	0.266500		0.0	0.0	0.266500		0.0	0.0	0.0
7	WDIA220	1	0.266500	0.266500		0.0	0.0	0.266500		0.0	0.0	0.0
8	WDRI222	1	0.286600	0.286600		0.0	0.0	0.286600		0.0	0.0	0.0
9	WSNG221U	1	0.325000	0.325000		0.0	0.0	0.325000		0.0	0.0	0.0
10	WSNG221D	1	0.363400	0.363400		0.0	0.0	0.363400		0.0	0.0	0.0
11	WDRI223	1	0.365000	0.365000		0.0	0.0	0.365000		0.0	0.0	0.0
12	WWCM220U	1	0.417000	0.417000		0.0	0.0	0.417000		0.0	0.0	0.0
13	WWCM220D	1	0.469000	0.469000		0.0	0.0	0.469000		0.0	0.0	0.0
14	WDRI224U	1	0.483500	0.483500		0.0	0.0	0.483500		0.0	0.0	0.0
15	WDIA221	1	0.483500	0.483500		0.0	0.0	0.483500		0.0	0.0	0.0
16	WDRI224D	1	0.610000	0.610000		0.0	0.0	0.610000		0.0	0.0	0.0
17	WBHZ220C	1	0.610000	0.610000		0.0	0.0	0.610000		0.0	0.0	0.0
END	BLL22U	1	0.610000	0.610000		0.0	0.0	0.610000		0.0	0.0	0.0
END	BLGWIL	1	0.610000	0.610000		0.0	0.0	0.610000		0.0	0.0	0.0

TOTAL LENGTH = 0.610000 ARC LENGTH = 0.610000
ERROR(X) = 0.0 ERROR(Y) = 0.0 ERROR(Z) = 0.610000D+00
ERROR(THETA) = 0.0 ERROR(PHI) = 0.0 ERROR(PSI) = 0.0

Appendix 1

Appendix 1

Gun W line

LIL W GEOMETRY OF OPTICAL ELEMENTS INTERSECTION AXES TO END SPECTR. "MAD" VERSION: 4.16 RUN: 27/05/86 19.06.12
SURVEY OF BEAM LINE "BLILS" PAGE 1

POS. NO.	ELEMENT NAME	OCC. NO.	SEQUENCE SUM(L) [M]	ARC [M]	I	POSITIONS X [M]	Y [M]	Z [M]	I	ANGLES THETA [RAD]	PHI [RAD]	PSI [RAD]
BEGIN	BLILS	1	0.0	0.0		0.0	0.0	0.0		0.0	0.0	0.0
BEGIN	BLILC	1	0.0	0.0		0.0	0.0	0.0		0.0	0.0	0.0
BEGIN	BLL22D	1	0.0	0.0		0.0	0.0	0.0		0.0	0.0	0.0
1	WBHZ220C	1	0.0	0.0		0.0	0.0	0.0		0.0	0.0	0.0
2	WDRI225	1	0.059500	0.059500		0.0	0.0	0.059500		0.0	0.0	0.0
3	WDVT222U	1	0.079500	0.079500		0.0	0.0	0.079500		0.0	0.0	0.0
4	WDVT222D	1	0.099500	0.099500		0.0	0.0	0.099500		0.0	0.0	0.0
5	WDRI226	1	0.153500	0.153500		0.0	0.0	0.153500		0.0	0.0	0.0
6	WSNG222U	1	0.191900	0.191900		0.0	0.0	0.191900		0.0	0.0	0.0
7	WSNG222D	1	0.230300	0.230300		0.0	0.0	0.230300		0.0	0.0	0.0
8	WDRI227	1	0.245000	0.245000		0.0	0.0	0.245000		0.0	0.0	0.0
9	WUMA220U	1	0.313000	0.313000		0.0	0.0	0.313000		0.0	0.0	0.0
10	WUMA220D	1	0.375000	0.375000		0.0	0.0	0.375000		0.0	0.0	0.0
11	WDRI228	1	0.404400	0.404400		0.0	0.0	0.404400		0.0	0.0	0.0
12	WDVT223U	1	0.424400	0.424400		0.0	0.0	0.424400		0.0	0.0	0.0
13	WDVT223D	1	0.444400	0.444400		0.0	0.0	0.444400		0.0	0.0	0.0
14	WDRI229	1	0.475000	0.475000		0.0	0.0	0.475000		0.0	0.0	0.0
END	BLL22D	1	0.475000	0.475000		0.0	0.0	0.475000		0.0	0.0	0.0
BEGIN	BLL23	1	0.475000	0.475000		0.0	0.0	0.475000		0.0	0.0	0.0
15	WDRI231	1	0.531000	0.531000		0.0	0.0	0.531000		0.0	0.0	0.0
16	WPBW220C	1	0.531000	0.531000		0.0	0.0	0.531000		0.0	0.0	0.0
17	WDRI232	1	0.585000	0.585000		0.0	0.0	0.585000		0.0	0.0	0.0
18	WSNG230U	1	0.623400	0.623400		0.0	0.0	0.623400		0.0	0.0	0.0
19	WSNG230D	1	0.661800	0.661800		0.0	0.0	0.661800		0.0	0.0	0.0
20	WDRI233	1	0.720800	0.720800		0.0	0.0	0.720800		0.0	0.0	0.0
21	WSNW230	1	1.014800	1.014800		0.0	0.0	1.014800		0.0	0.0	0.0
22	WDRI234	1	1.045000	1.045000		0.0	0.0	1.045000		0.0	0.0	0.0
23	WBNW230C	1	1.045000	1.045000		0.0	0.0	1.045000		0.0	0.0	0.0
24	WDRI235	1	1.258000	1.258000		0.0	0.0	1.258000		0.0	0.0	0.0
END	BLL23	1	1.258000	1.258000		0.0	0.0	1.258000		0.0	0.0	0.0
BEGIN	BLL25	1	1.258000	1.258000		0.0	0.0	1.258000		0.0	0.0	0.0
25	WDRI251	1	1.278300	1.278300		0.0	0.0	1.278300		0.0	0.0	0.0
26	WSNT250U	1	1.328500	1.328500		0.0	0.0	1.328500		0.0	0.0	0.0
27	WSNT250D	1	1.378700	1.378700		0.0	0.0	1.378700		0.0	0.0	0.0
28	WDRI252	1	1.408000	1.408000		0.0	0.0	1.408000		0.0	0.0	0.0
29	WUMA250U	1	1.476000	1.476000		0.0	0.0	1.476000		0.0	0.0	0.0
30	WUMA250D	1	1.538000	1.538000		0.0	0.0	1.538000		0.0	0.0	0.0
31	WDRI253	1	1.778500	1.778500		0.0	0.0	1.778500		0.0	0.0	0.0
32	WUPH250C	1	1.778500	1.778500		0.0	0.0	1.778500		0.0	0.0	0.0
33	WDRI254	1	1.941000	1.941000		0.0	0.0	1.941000		0.0	0.0	0.0
34	WWBS250C	1	1.941000	1.941000		0.0	0.0	1.941000		0.0	0.0	0.0
35	WDRI255	1	2.070000	2.070000		0.0	0.0	2.070000		0.0	0.0	0.0
36	WCEP250C	1	2.070000	2.070000		0.0	0.0	2.070000		0.0	0.0	0.0
37	WDRI256	1	2.071000	2.071000		0.0	0.0	2.071000		0.0	0.0	0.0
38	WCEP250	1	2.078000	2.078000		0.0	0.0	2.078000		0.0	0.0	0.0
END	BLL25	1	2.078000	2.078000		0.0	0.0	2.078000		0.0	0.0	0.0
END	BLILC	1	2.078000	2.078000		0.0	0.0	2.078000		0.0	0.0	0.0
BEGIN	BLLS	1	2.078000	2.078000		0.0	0.0	2.078000		0.0	0.0	0.0
39	WDRI257U	1	2.358000	2.358000		0.0	0.0	2.358000		0.0	0.0	0.0
40	WDVT251S	1	2.498000	2.498000		0.0	0.0	2.498000		0.0	0.0	0.0

LIL W GEOMETRY OF OPTICAL ELEMENTS INTERSECTION AXES TO END SPECTR. "MAD" VERSION: 4.16 RUN: 27/05/86 19.06.12
SURVEY OF BEAM LINE "BLILS" PAGE 2

POS. NO.	ELEMENT NAME	OCC. NO.	SEQUENCE SUM(L) [M]	ARC [M]	I	POSITIONS X [M]	Y [M]	Z [M]	I	ANGLES THETA [RAD]	PHI [RAD]	PSI [RAD]
41	WDRI257D	1	3.490000	3.490000		0.0	0.0	3.490000		0.0	0.0	0.0
42	WWCM25SU	1	3.542000	3.542000		0.0	0.0	3.542000		0.0	0.0	0.0
43	WWCM25SD	1	3.594000	3.594000		0.0	0.0	3.594000		0.0	0.0	0.0
44	WDRI258	1	3.820000	3.820000		0.0	0.0	3.820000		0.0	0.0	0.0
45	WBHZ25S	1	4.449600	4.449600		0.234792	0.0	4.386839		0.785398	0.0	0.0
46	WDRI259U	1	4.649600	4.649600		0.376214	0.0	4.528261		0.785398	0.0	0.0
47	WDVT252S	1	4.789600	4.789600		0.475209	0.0	4.627256		0.785398	0.0	0.0
48	WDRI259D	1	5.929600	5.929600		1.281310	0.0	5.433357		0.785398	0.0	0.0
END	BLLS	1	5.929600	5.929600		1.281310	0.0	5.433357		0.785398	0.0	0.0
END	BLILS	1	5.929600	5.929600		1.281310	0.0	5.433357		0.785398	0.0	0.0

TOTAL LENGTH =	5.929600	ARC LENGTH =	5.929600		
ERROR(X) =	0.128131D+01	ERROR(Y) =	0.0	ERROR(Z) =	0.543336D+01
ERROR(THETA) =	0.785398D+00	ERROR(PHI) =	0.0	ERROR(PSI) =	0.0

LIL-W injection Line

Appendix 1

"MAD" VERSION 4.16

DATE AND TIME OF THIS RUN: 27/05/86 19.06.12

INPUT STREAM AND MESSAGE LOG:

```
         TITLE
         LIL - W   Geometry of optical elements    Gun W to spectrometer end     27.05.86
         WGUN210   : DRIFT, L=0.0550                ! CATHODE TO ANODE EXIT +- 1MM
         WDRI211   : DRIFT, L=0.0414
    5    WDVT221U  : HKICK, L=0.0200                !?LENGTH OF YOKE
         WDVT221D  : HKICK, L=0.0200                !?LENGTH OF YOKE
         WDRI212   : DRIFT, L=0.1226                !-
         WDRI221   : DRIFT, L=0.0075
         WDIA220   : MARKER                         ! DIAPHRAGMA L=+- 1MM, R=12.5 MM
   10    WDRI222   : DRIFT, L=0.0201
         WSNG221U  : SOLENOID, L=0.0384, KS=2.731   ! OPTICAL LENGTH AT 60 KEV
         WSNG221D  : SOLENOID, L=0.0384, KS=2.731   ! OPTICAL LENGTH AT 60 KEV
         WDRI223   : DRIFT, L=0.0016
         WWCM220U  : MONITOR,  L=0.0520             ! MECH. LENGTH + 2MM FOR HALF-GASKET
   15    WWCM220D  : MONITOR,  L=0.0520             ! MECH. LENGTH + 2MM FOR HALF-GASKET
         WDRI224U  : DRIFT, L=0.0145
         WDIA221   : MARKER                         ! DIAPHRAGMA L=+-2.5MM R=2.5MM
         WDRI224D  : DRIFT, L=0.1265
         WBHZ220C  : MARKER                         !-INTERSECTION OF AXES  ANGLE=75.DEGR
   20    WDRI225   : DRIFT, L=0.0595
         WDVT222U  : HKICK, L=0.020                 !?LENGTH OF YOKE
         WDVT222D  : HKICK, L=0.020                 !?LENGTH OF YOKE
         WDRI226   : DRIFT, L=0.0540
         WSNG222U  : SOLENOID, L=0.0384, KS=2.731   !?OPTICAL LENGTH
   25    WSNG222D  : SOLENOID, L=0.0384, KS=2.731   !?OPTICAL LENGTH
         WDRI227   : DRIFT, L=0.0147
         WUMA220U  : MONITOR,  L=0.0680             ! MECH. LENGTH + 2MM FOR HALF-GASKET
         WUMA220D  : MONITOR,  L=0.0620             ! MECH. LENGTH + 2MM FOR HALF-GASKET
         WDRI228   : DRIFT, L=0.0294
   30    WDVT223U  : HKICK, L=0.0200                !?LENGTH OF YOKE
         WDVT223D  : HKICK, L=0.0200                !?LENGTH OF YOKE
         WDRI229   : DRIFT, L=0.0306                !
         WDRI231   : DRIFT, L=0.0560
         WPBW220C  : MARKER                         ! COUPLER AXIS PBW220
   35    WDRI232   : DRIFT, L=0.0540
         WSNG230U  : SOLENOID, L=0.0384, KS=2.731   !?OPTICAL LENGTH AT 60 KEV
         WSNG230D  : SOLENOID, L=0.0384, KS=2.731   !?OPTICAL LENGTH AT 60 KEV
         WDRI233   : DRIFT, L=0.0590
         WSNW230   : DRIFT, L=0.2940                ! LENGTH OF IRON YOKE
   40    WDRI234   : DRIFT, L=0.0302
         WBNW230C  : MARKER                         ! COUPLER AXIS BNW230
         WDRI235   : DRIFT, L=0.2130                !-
         WDRI251   : DRIFT, L=0.0203
         WSNT250D  : SOLENOID, L=0.0502, KS=1.      !?OPTICAL LENGTH AT 4 MEV
   45    WSNT250U  : SOLENOID, L=0.0502, KS=1.      !?OPTICAL LENGTH AT 4 MEV
         WDRI252   : DRIFT, L=0.0293
         WUMA250U  : MONITOR,  L=0.0680             ! MECH. LENGTH + 2MM FOR HALF-GASKET
         WUMA250D  : MONITOR,  L=0.0620             ! MECH. LENGTH + 2MM FOR HALF-GASKET
         WDRI253   : DRIFT, L=0.2405
   50    WUPH250C  : MARKER                         !?COUPLER AXIS OF UPH 25
         WDRI 254  : DRIFT, L=0.1625
         WWBS250C  : MONITOR                        ! CENTRE WIRE




         WDRI255   : DRIFT, L=0.1290
         WCEP250C  : MARKER                         ! CENTRE TARGET ARM
   55    WDRI256   : DRIFT, L=0.0010
         WCEP250   : DRIFT, L=0.0070                !-CONVERTER TARGET
         WDRI257U  : DRIFT, L=0.280
         WDVT251S  : DRIFT, L=0.140
         WDRI257D  : DRIFT, L=0.992
   60    WWCM25SU  : MONITOR,  L=0.0520             ! MECH. LENGTH + 2MM FOR HALF-GASKET
         WWCM25SD  : MONITOR,  L=0.0520             ! MECH. LENGTH + 2MM FOR HALF-GASKET
         WDRI258   : DRIFT, L=0.2260
         WBHZ25S   : SBEND, L=0.6296,ANGLE=-0.785398   ! OPTICAL LENGTH
         WDRI259U  : DRIFT, L=0.200
   65    WDVT252S  : VKICK, L=0.140
         WDRI259D  : DRIFT, L=1.140
         WMSH25SC  : MONITOR
         TITLE
```

Sequence and length of elements

(MAD input)

Appendix 1

REFERENCES

1) G. Le Meur, Note LAL/PI 82-67/T (1982)

2) G. Le Meur, Note LAL/PI 83-08/T (1983)

3) J. Le Duff, letter to K. Hübner (20.3.84)

4) J.C. Bourdon, priv. comm. of PARMELA results (21.2.86)

5) A. Riche, LIL Meeting 5.2.86

6) K. Hübner, PS/LPI Note 85-32 (1985)

7) W. Heinze, PS/CO/WP 85-072 (1985)

8) R. Bonzano, B. Nicolai and A. Ruon, PS/EA/TS/Memo 85-35 (1985)

9) J.C. Bourdon, "Calcul de l'impedance shunt du pregroupeur", priv. comm. (21.1.86).

10) J.C. Bourdon and J. Rodier, Note LAL/PI 86-3/T (1986) and priv. comm., (22.1.86).

11) J.C. Bourdon and J. Rodier, "Réglage de cellules du groupeur W et résultats expérimentaux", Note LAL-PI 86-8/T (1986)

12) J.C. Bourdon, priv. comm. (8.1.86)

13) J.C. Bourdon, "Champ maximum dans le groupeur e^- W", priv. comm. (9.1.85).

14) B. Frammery, memorandum PS/OP/BF (25.3.86).

15) G. Le Meur, Note SA No 10/81 (12.10.81) and manuscript attached to it.

16) A. Bellanger, "Etalonnage des sondes Hall" (8.1.85) and "Calibration aimant d'analyse" (22.1.86)

17) R. Belbéoch, LAL/PI 85-18/T (1985)

18) R. Chaput, LAL/PI 85-20/T (1985)
S. Kulinski, PS/LPI Note 85-11 (1985)
S. Kulinski and A. Riche, PS/LPI Note 85-40 (1986)

19) R. Belbéoch, LAL/PI 84-11/T (1984);
P. Brunet and R. Chaput, Proc. Lin. Acc. Conf., Seeheim (1984) 189

20) J.C. Sheppard, J.E. Clendelin, R.H. Helm, M.J. Lee, R.H. Miller and C.A. Blocker, IEEE Transactions on Nucl Sci., NS-30 (1983) 2161.

Figure Captions

Fig. 1 Sketch of layout

Fig. 2 Energy gain and peak electric field in prebuncher W versus attenuator settings.

Fig. 3 Reflected power of buncher W versus frequency for three different temperatures.

Fig. 4 Measured energy gain ΔW_1 squared versus power dissipated in buncher W. Straight line: calculated energy gain ΔW_2.

Fig. 5 Momentum distribution at the SEM grid $\bar{p}$ = 4.56 MeV/c, $\delta p/p$ = 0.30%, $\Delta p/p$ (FWbase) = 1.56%; $\Delta W_{p\beta}$ = 27 keV, ϕ = 55 mm, I(WCM25.S)=17mA
Base line assumed marked by the two horizontal arrows.

Fig. 6 Momentum distribution at the SEM grid $\bar{p}$ = 4.60 MeV/c, $\delta p/p$ = 0.28%, $\Delta p/p$ (FWbase) = 1.40%, $\Delta W_{p\beta}$ = 25 keV, ϕ = 53 mm, I(WCM25.S)=17mA.

Fig. 7 Momentum distributions at the SEM grid at constant settings recorded within 20 min.
$\bar{p}$ = 3.90 MeV/c, $\Delta W_{p\beta}$ = 27 keV, ϕ = 52 mm, I(WCM25.S) = 19 mA
Parameters of c): $\delta p/p$ = 0.39%, $\Delta p/p$ (FWbase) = 2.5%

Fig. 8 Attenuator setting versus phase shifter for minimum spectrum width. Fitted straight line ΔW(keV) = 14 ϕ (degree) - 76 or A = ϕ (mm) + 375.

Fig. 9 Peak current after buncher at UMA25 versus phase shifter position with various attenuations of prebuncher.

Fig. 10 Locus of maximum current at WCM25.S in the prebuncher phase, attenuator plane. Attenuation increased by 4.1 db cable.
WCM22 = 150 mA, $\bar{p} \approx$ 4.6 MeV/c.

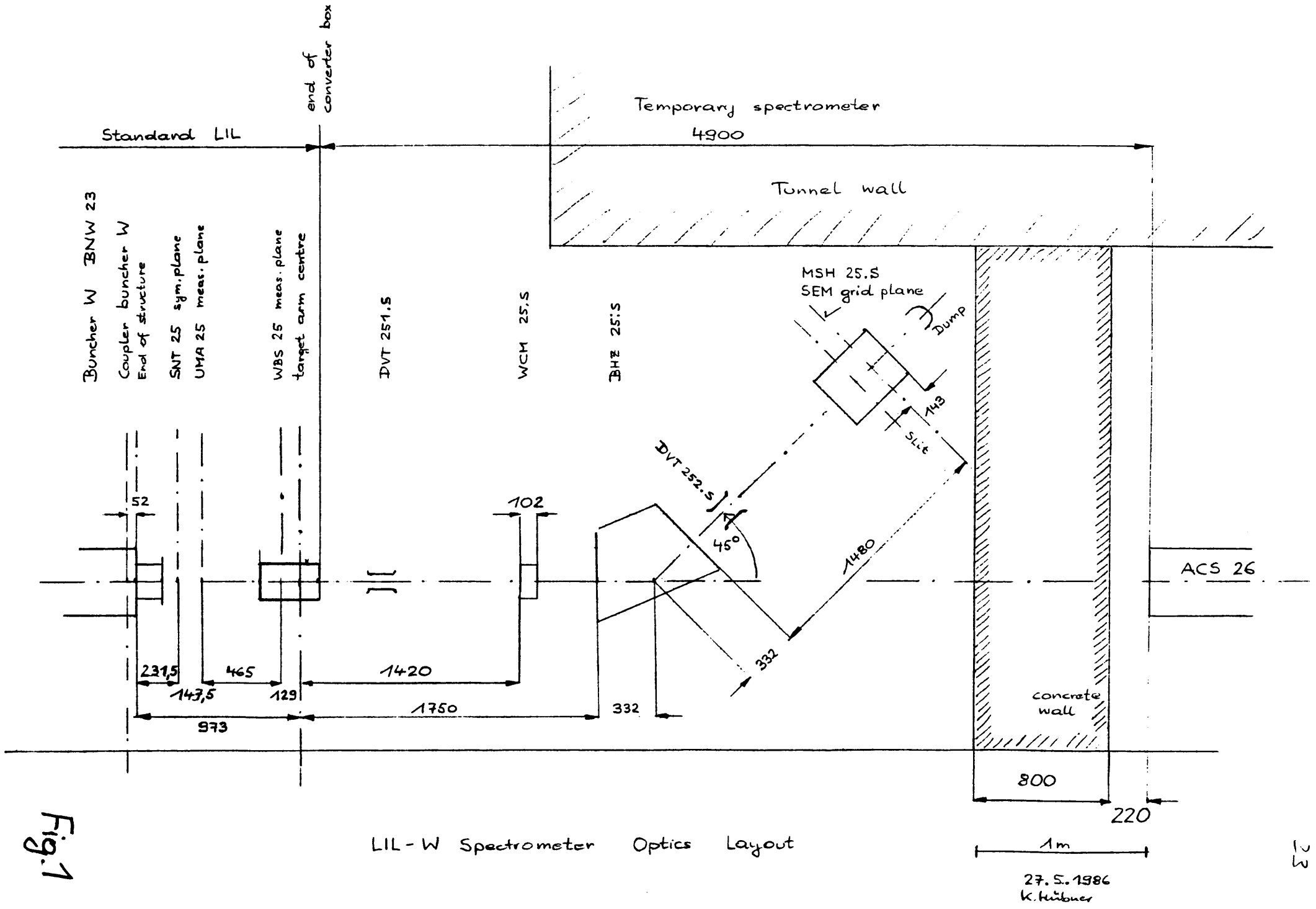

Fig. 1

LIL - W Spectrometer Optics Layout

27.5.1986
K. Hübner

Energy gain and peak field in prebuncher W versus attenuator settings.

for P(buncher) = 1 MW

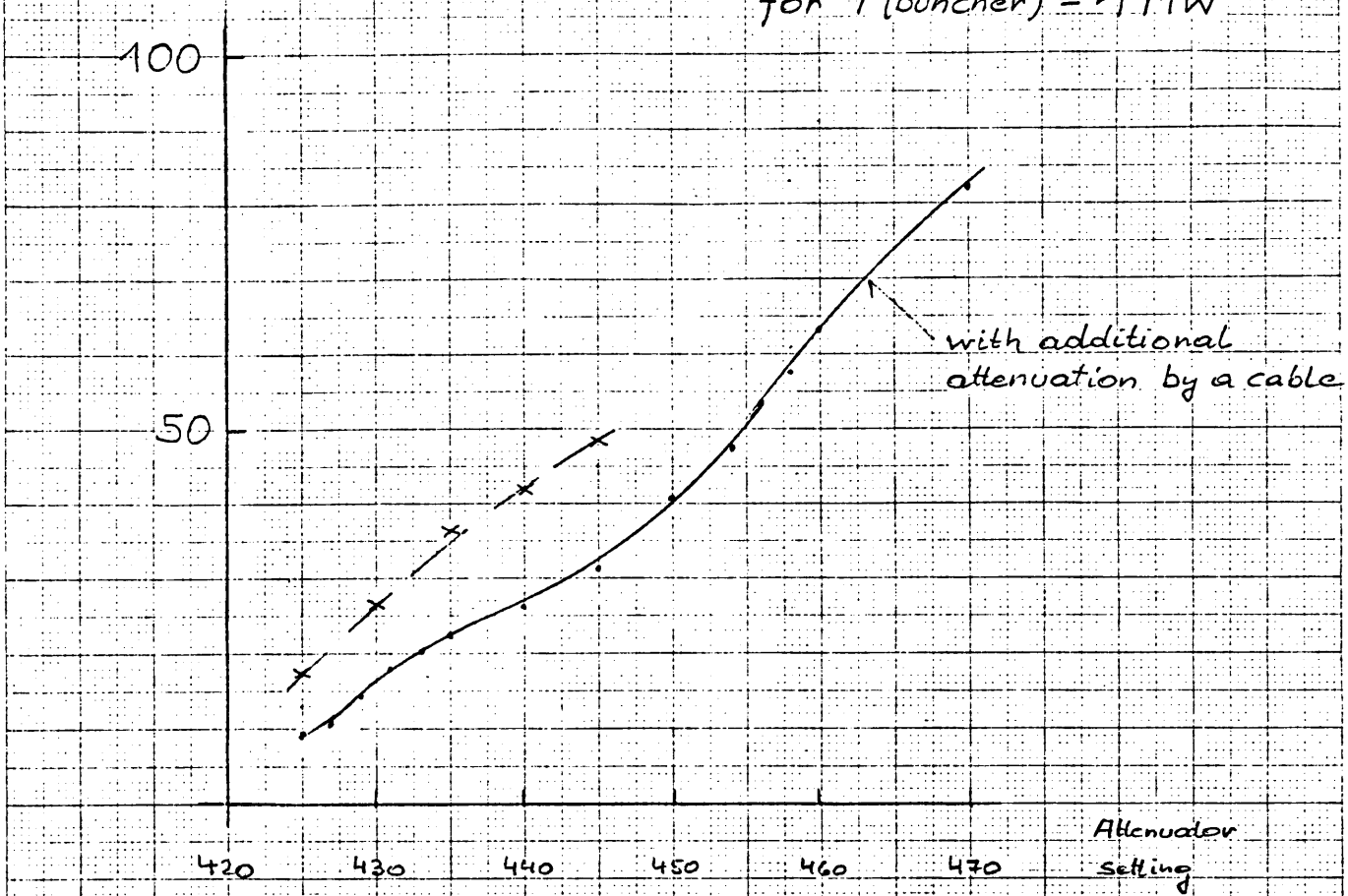

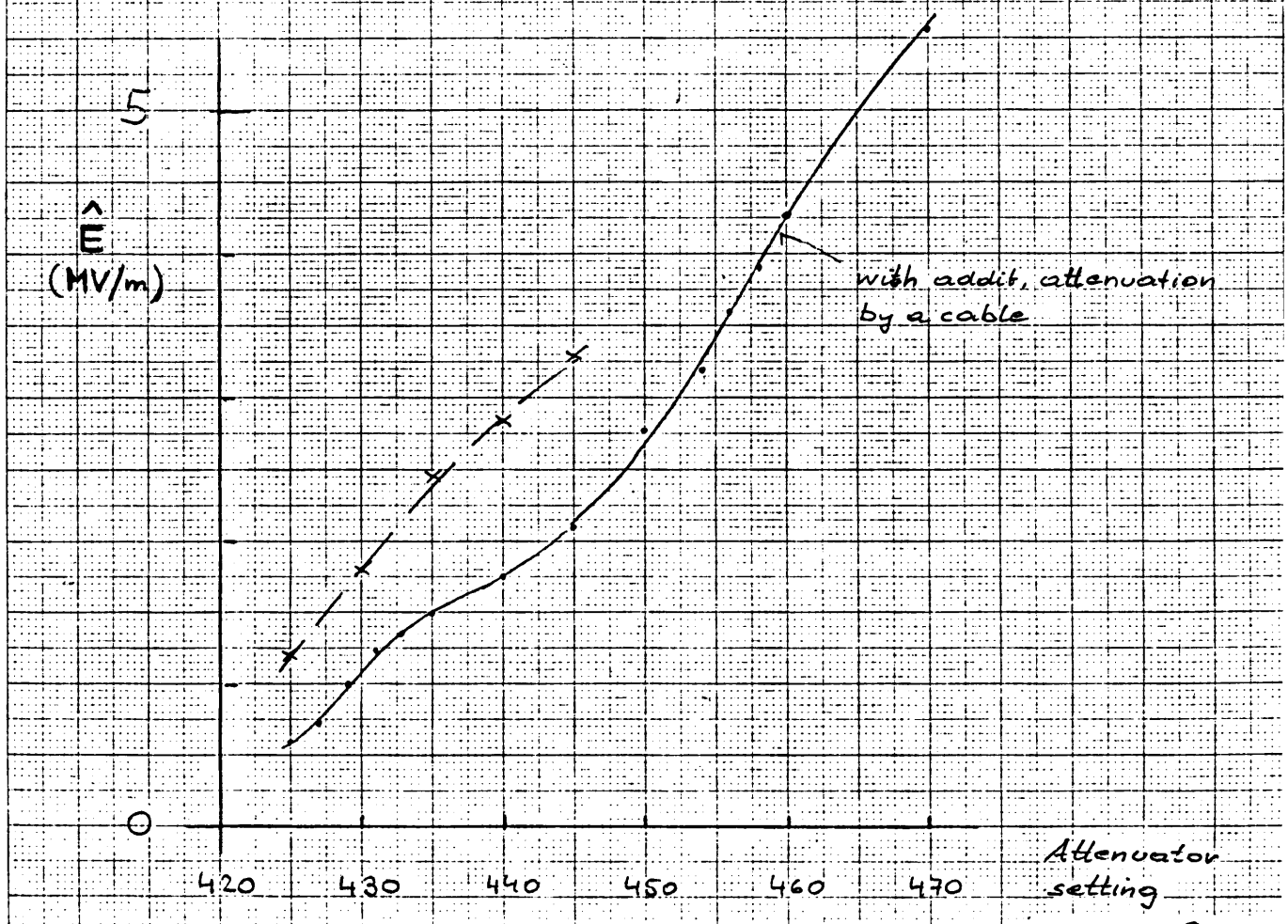

Fig. 2

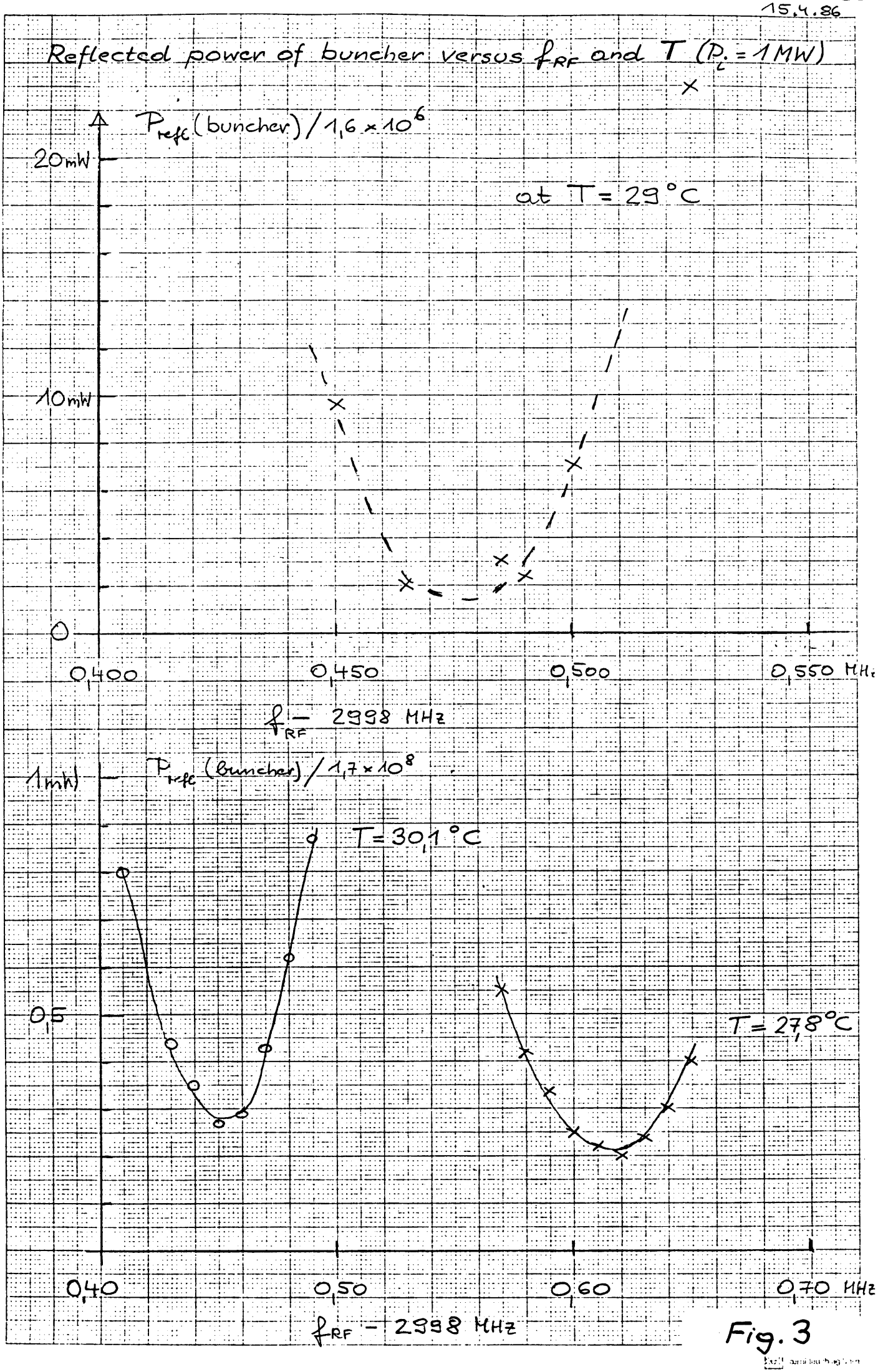
Reflected power of buncher versus f_{RF} and T (P_L = 1 MW)
P_{refl} (buncher) / $1,6 \times 10^6$
20 mW
10 mW
0
at T = 29 °C
0,400
0,450
0,500
0,550 MHz
f_{RF} – 2998 MHz
P_{refl} (buncher) / $1,7 \times 10^8$
1 mW
0,5
T = 30,1 °C
T = 27,8 °C
0,40
0,50
0,60
0,70 MHz
f_{RF} – 2998 MHz

Fig. 3

Fig. 3

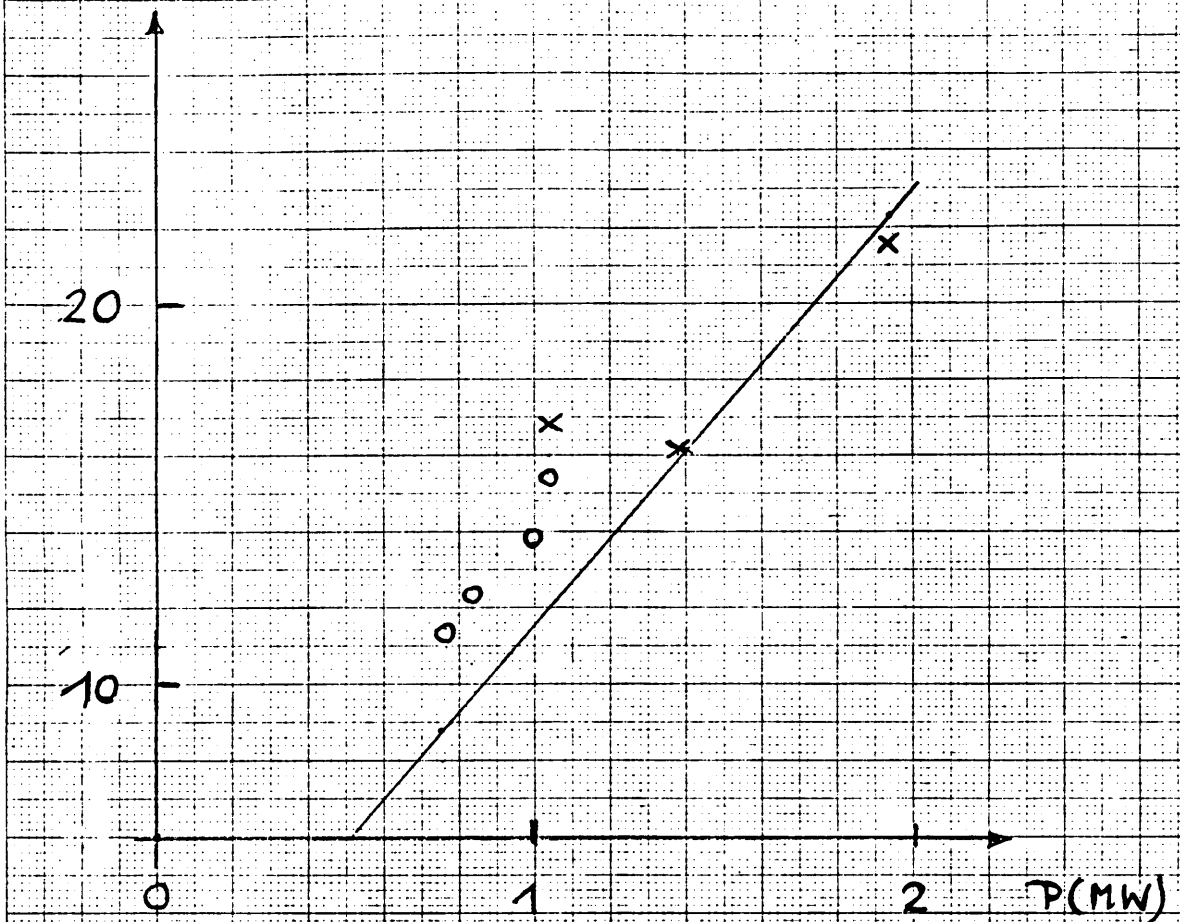

Fig. 4

Fig. 3 4

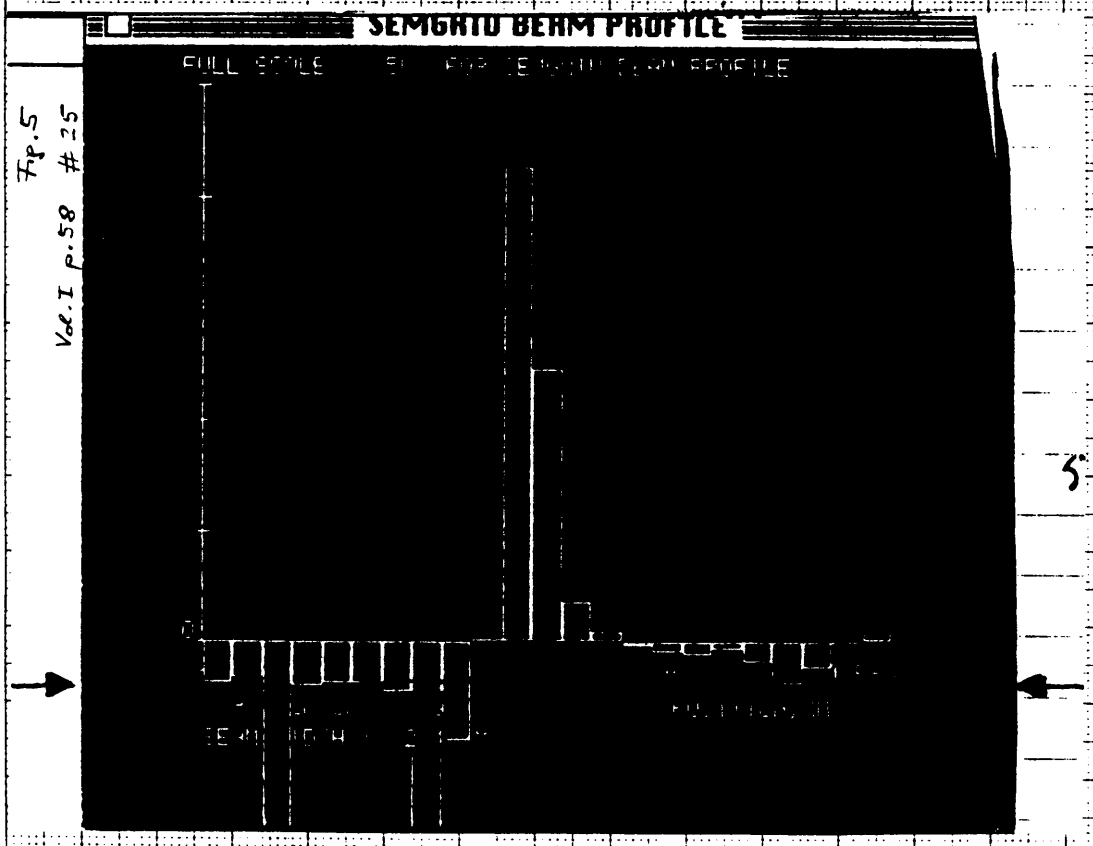

Fig. 5

Fig. 5
Vol. I p. 58 #25

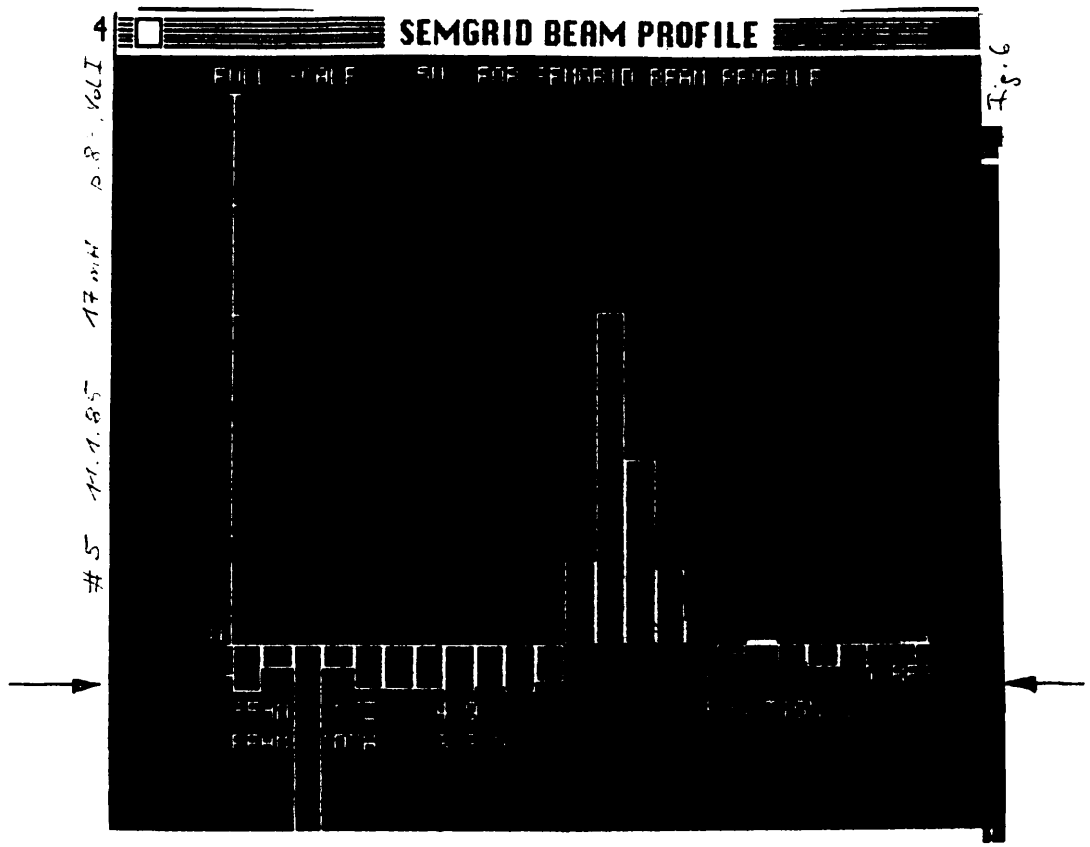
SEMGRID BEAM PROFILE
#5 11.1.85 17:11 Vol.I p.8

Fig.6

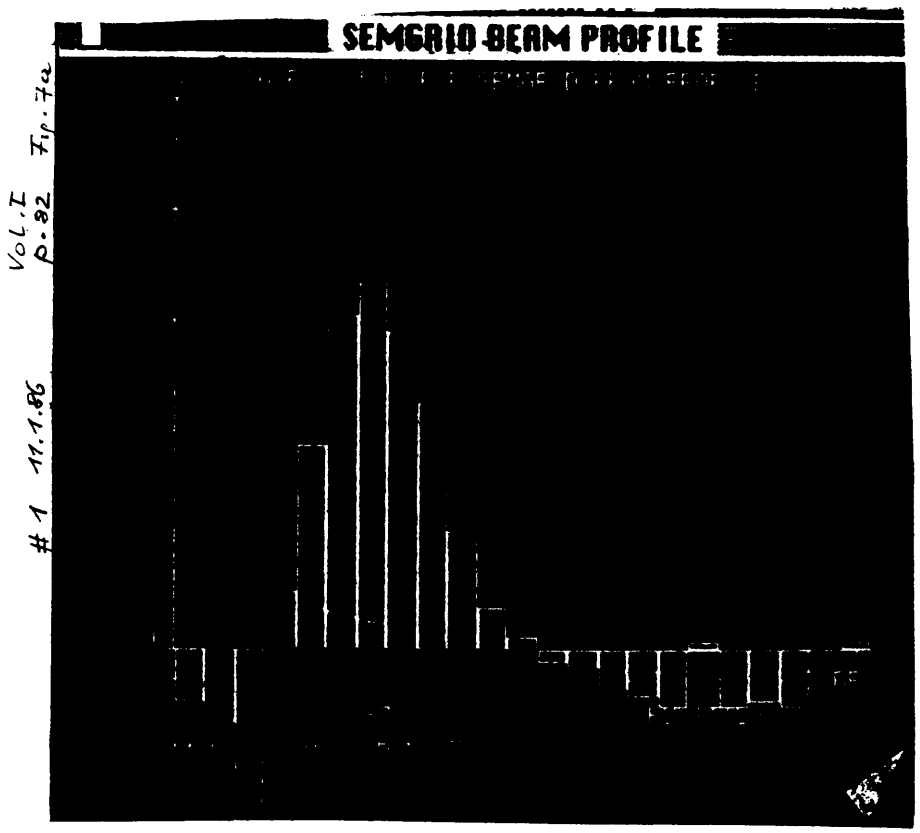
SEMGRID BEAM PROFILE
#1 11.1.86 Vol.I p.82

Fig.7a

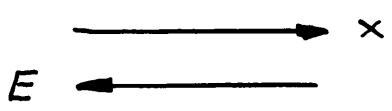
x
E

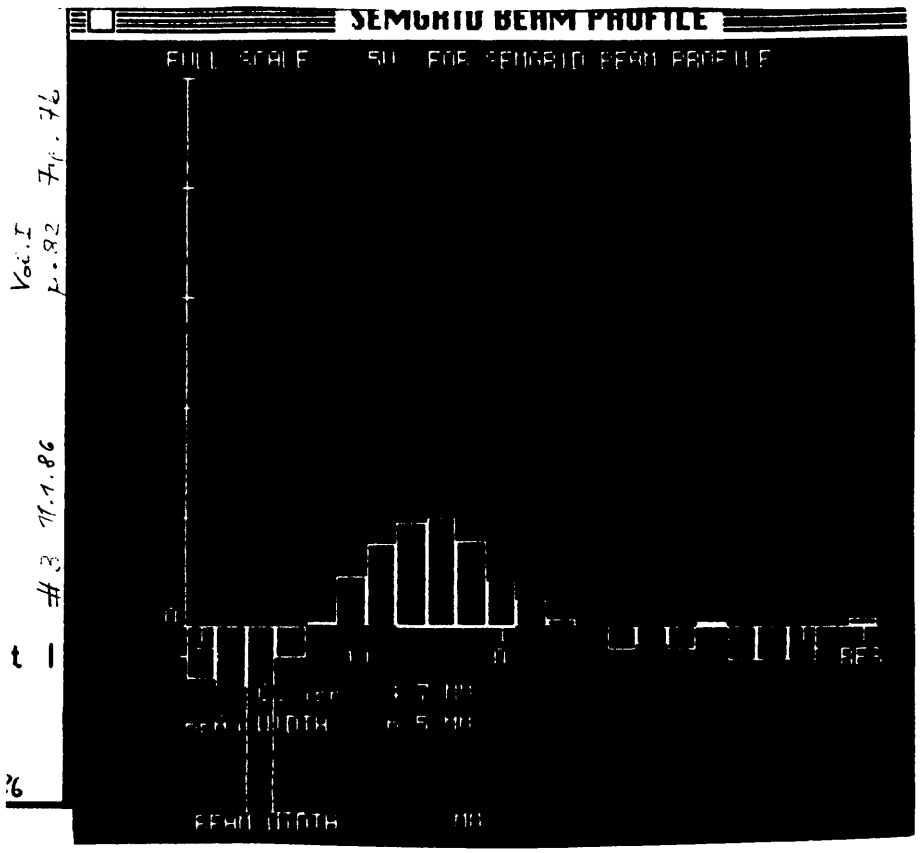

Fig. 7b

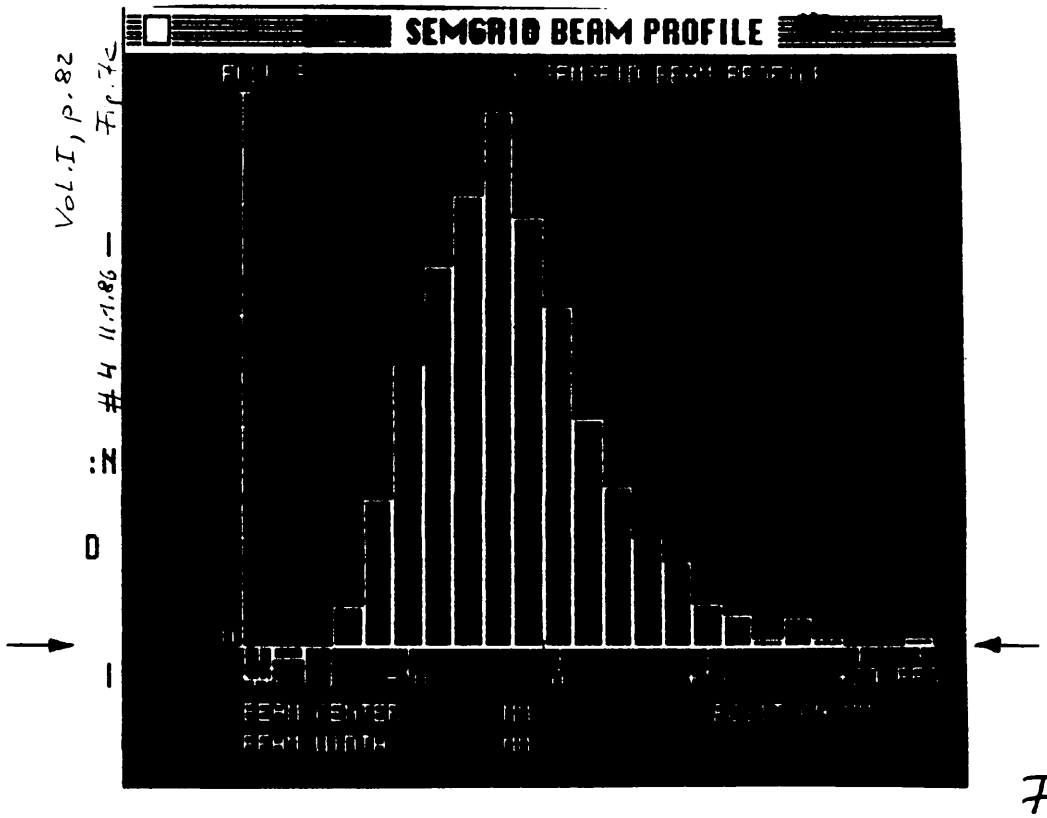

Fig. 7c

X

E

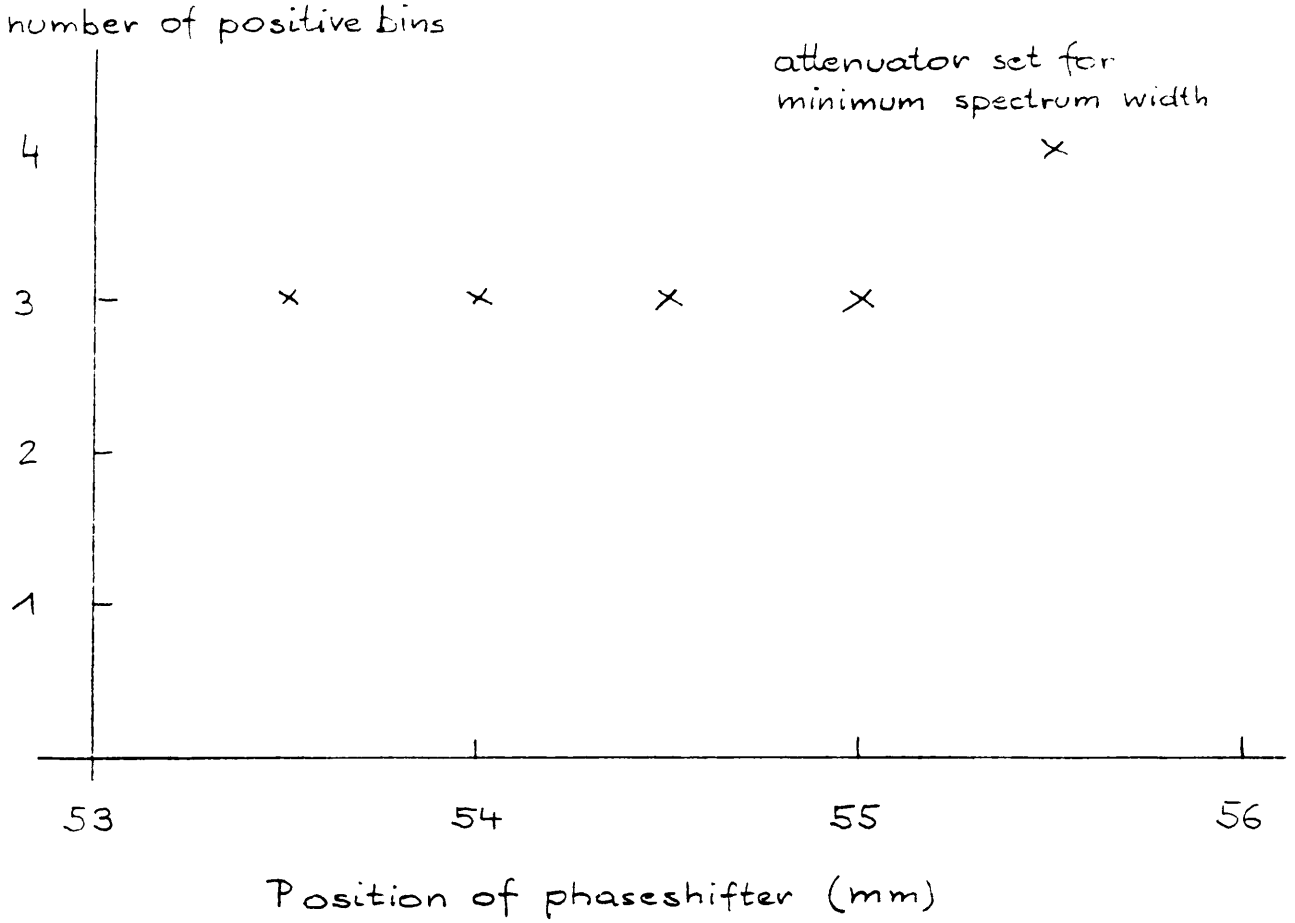
number of positive bins
attenuator set for
minimum spectrum width
4
3
2
1
53
54
55
56
Position of phaseshifter (mm)

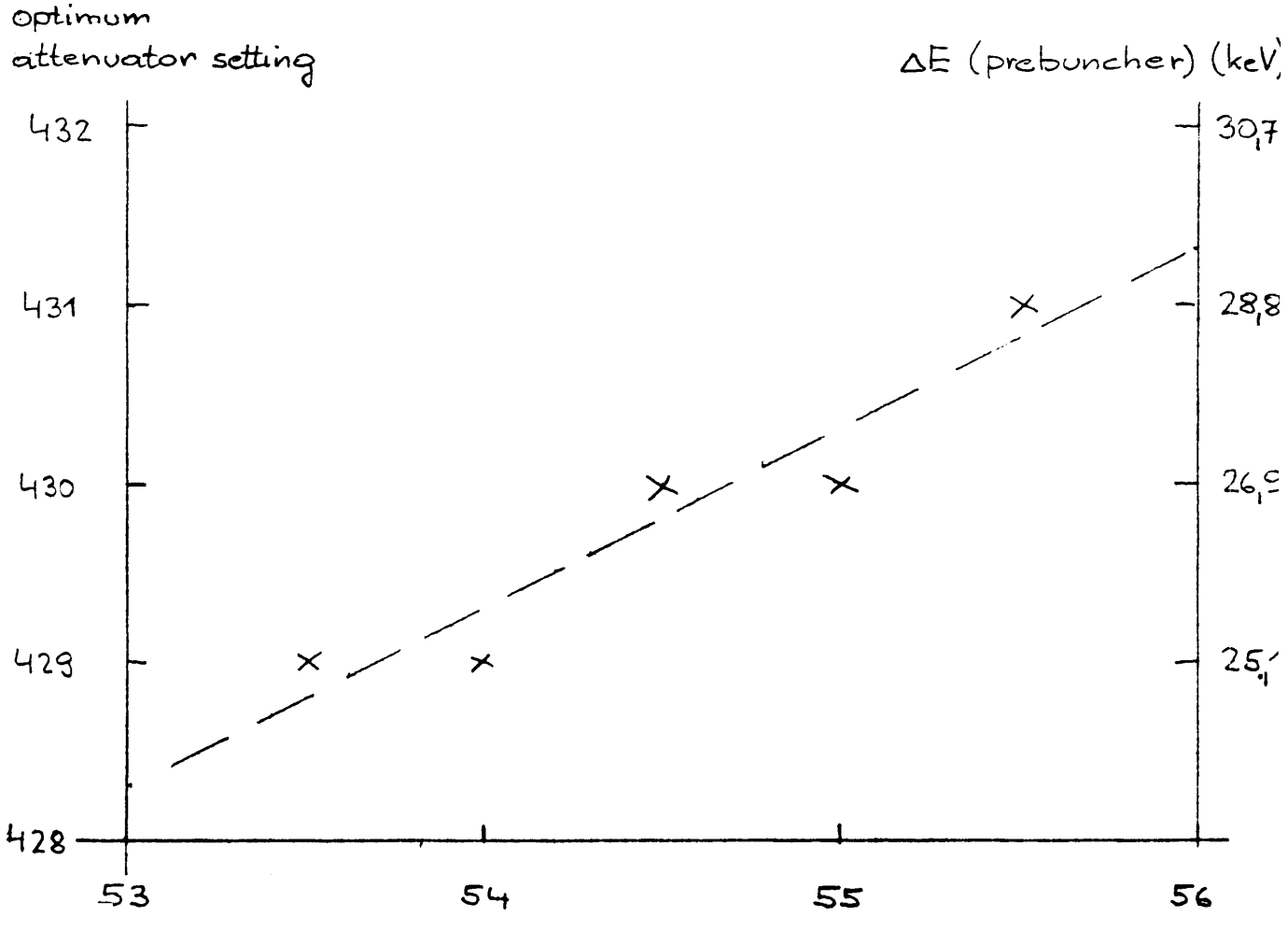
optimum
attenuator setting
ΔE (prebuncher) (keV)
432
431
430
429
428
30,7
28,8
26,9
25,1
53
54
55
56
Position of phaseshifter (mm)

Fig. 8

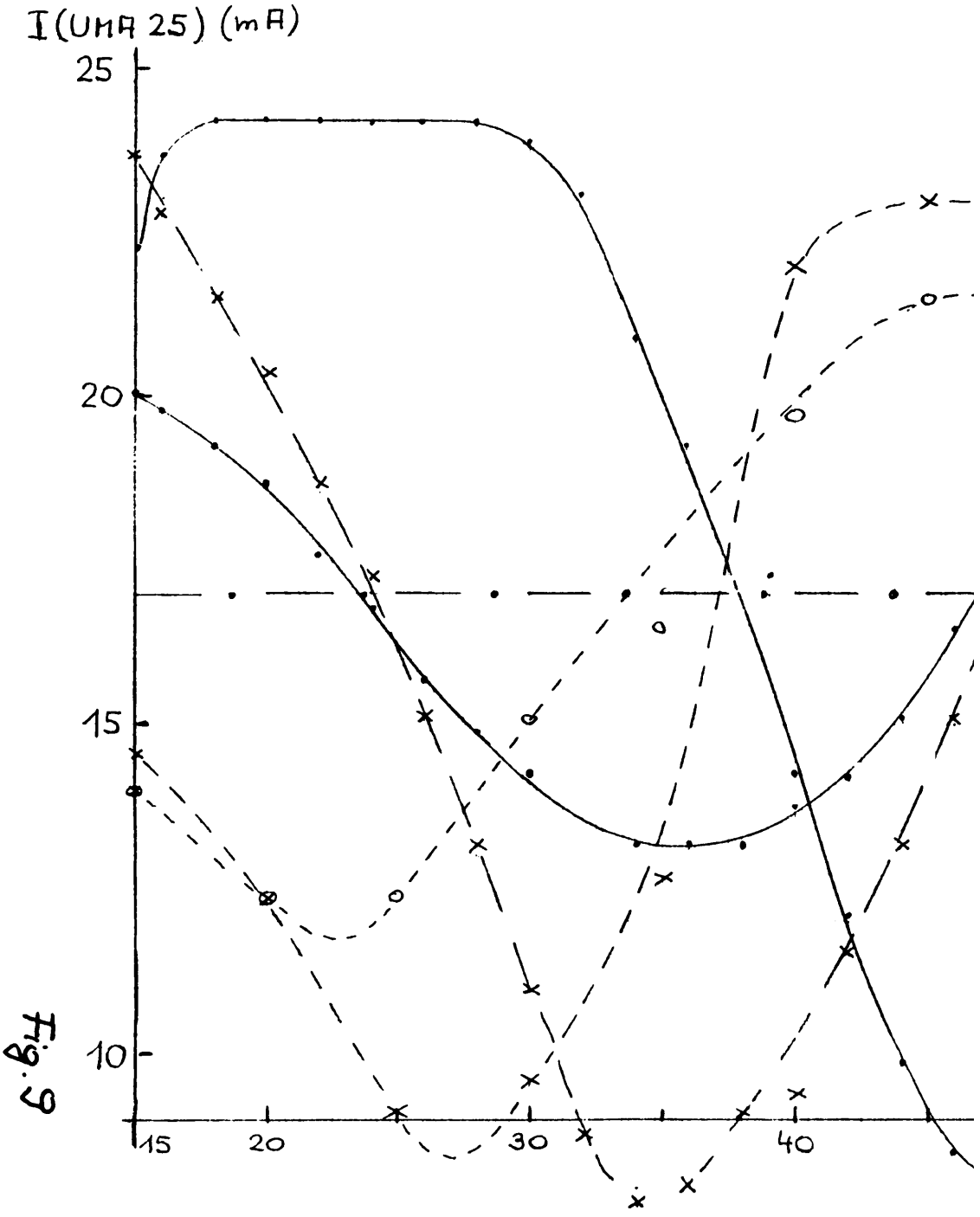

Fig. 9

23.4.86

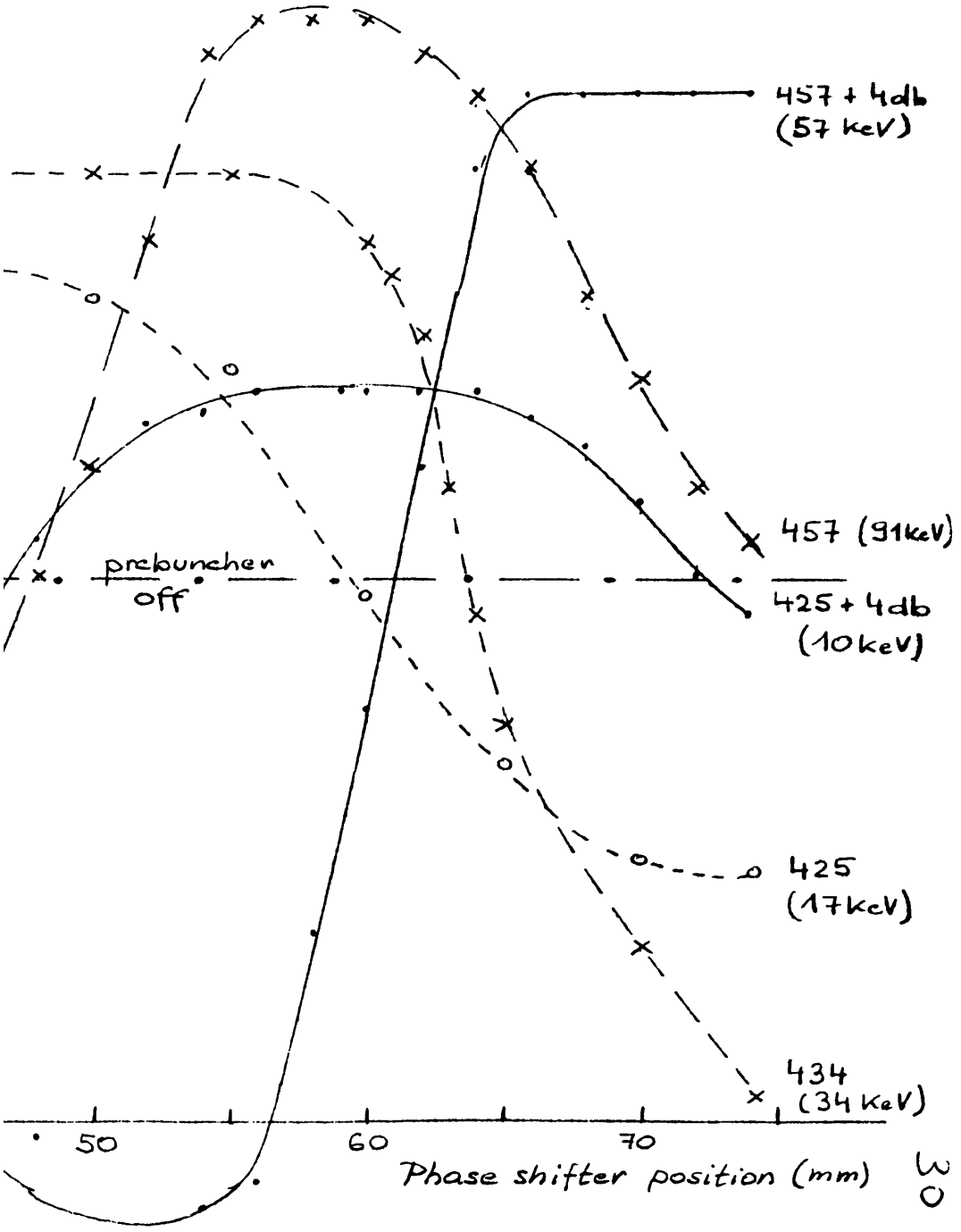
457 + 4db
(57 keV)
457 (91keV)
prebuncher
off
425 + 4db
(10keV)
425
(17keV)
434
(34 keV)
50
60
70
Phase shifter position (mm)
W
O

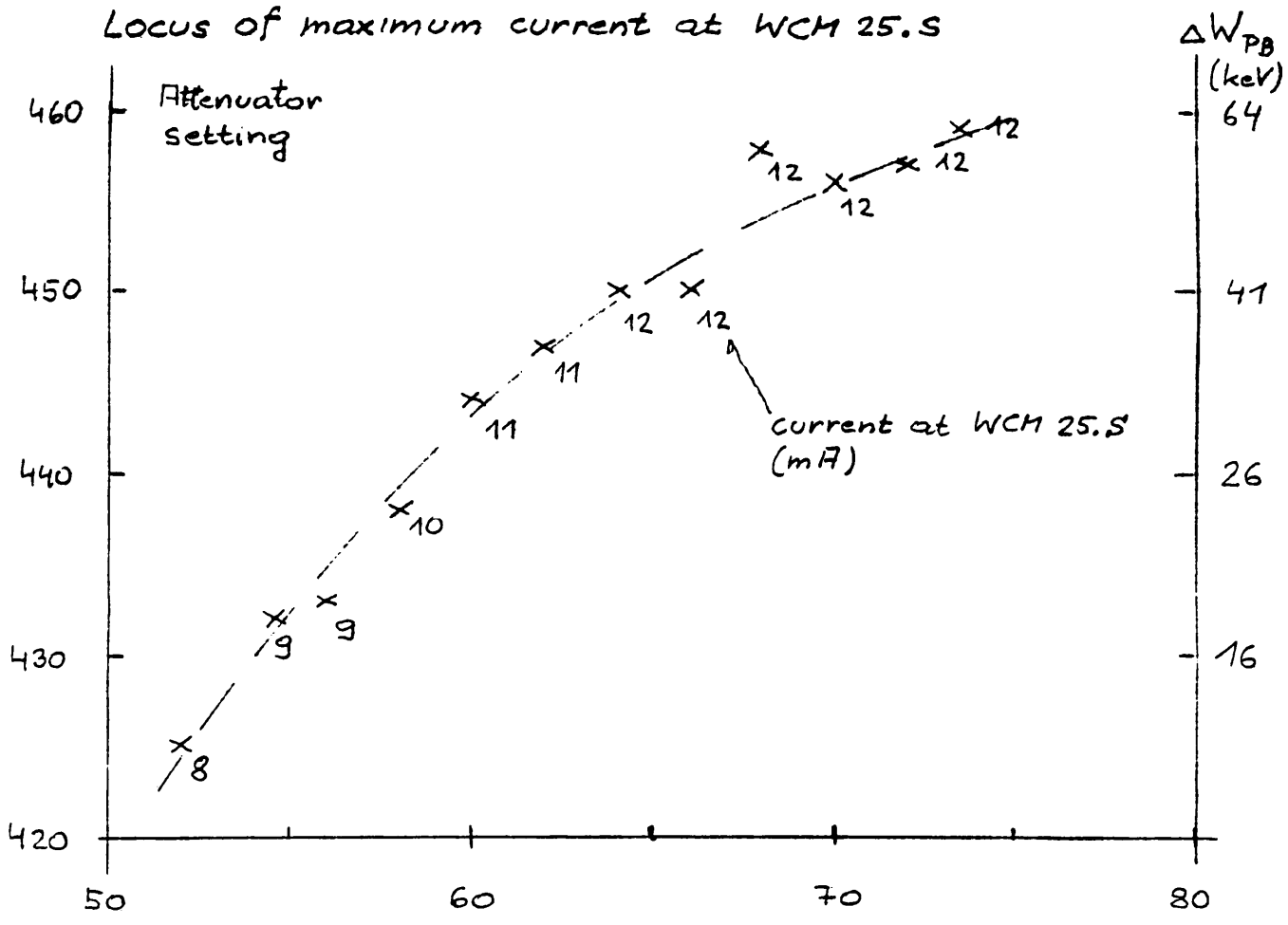
Locus of maximum current at WCM 25.S
ΔW PB (keV)
Attenuator setting
460
450
440
430
420
64
41
26
16
50
60
70
80
current at WCM 25.S (mA)
Position of phaseshifter (mm)

Fig. 10

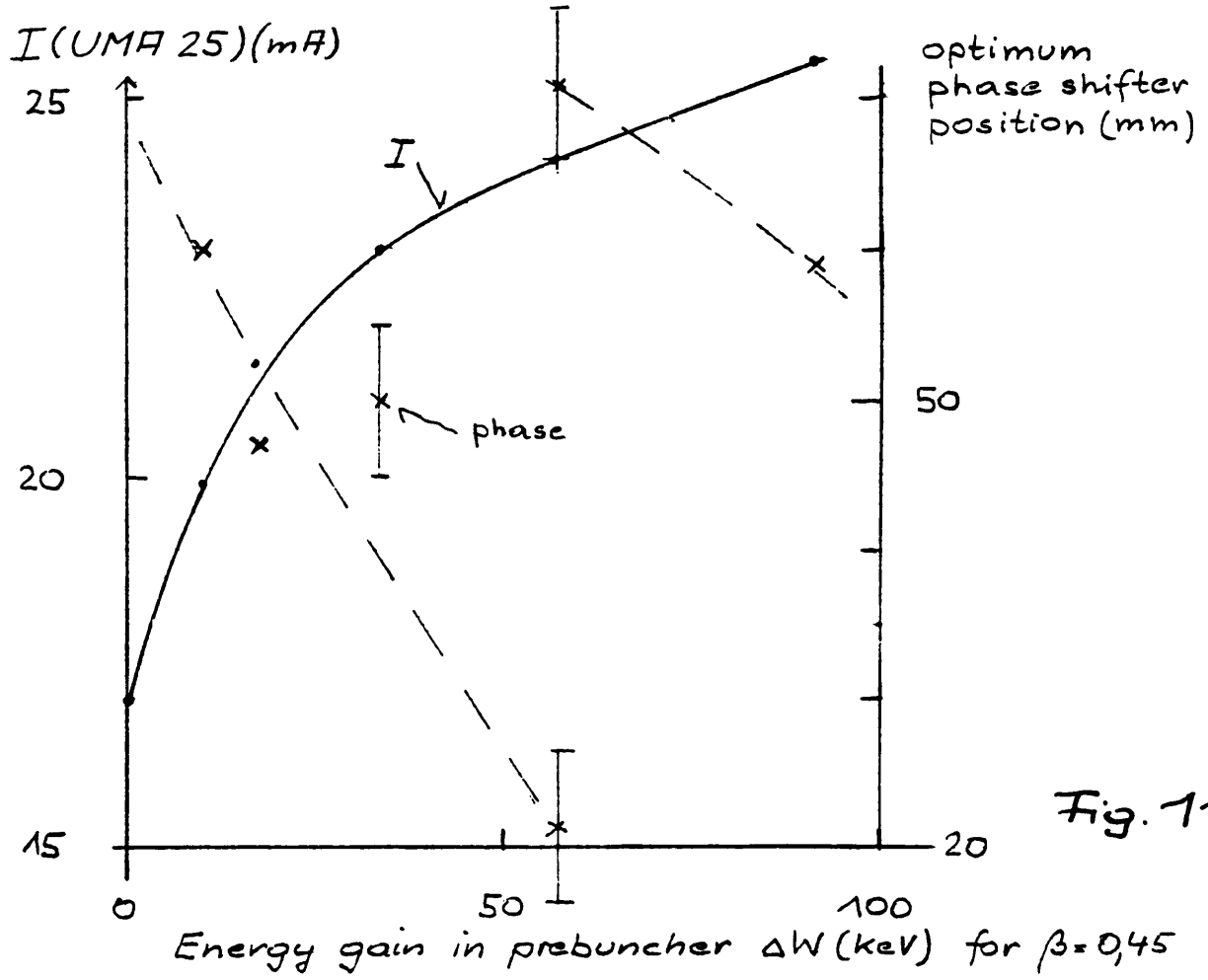
I (UMA 25) (mA)
optimum phase shifter position (mm)
25
20
15
I
phase
50
20
0
50
100
Energy gain in prebuncher ΔW (keV) for β = 0,45

Fig. 11

Beamsize (FWbase) at WBS 25 versus current in "telescope Lens" SNT 25

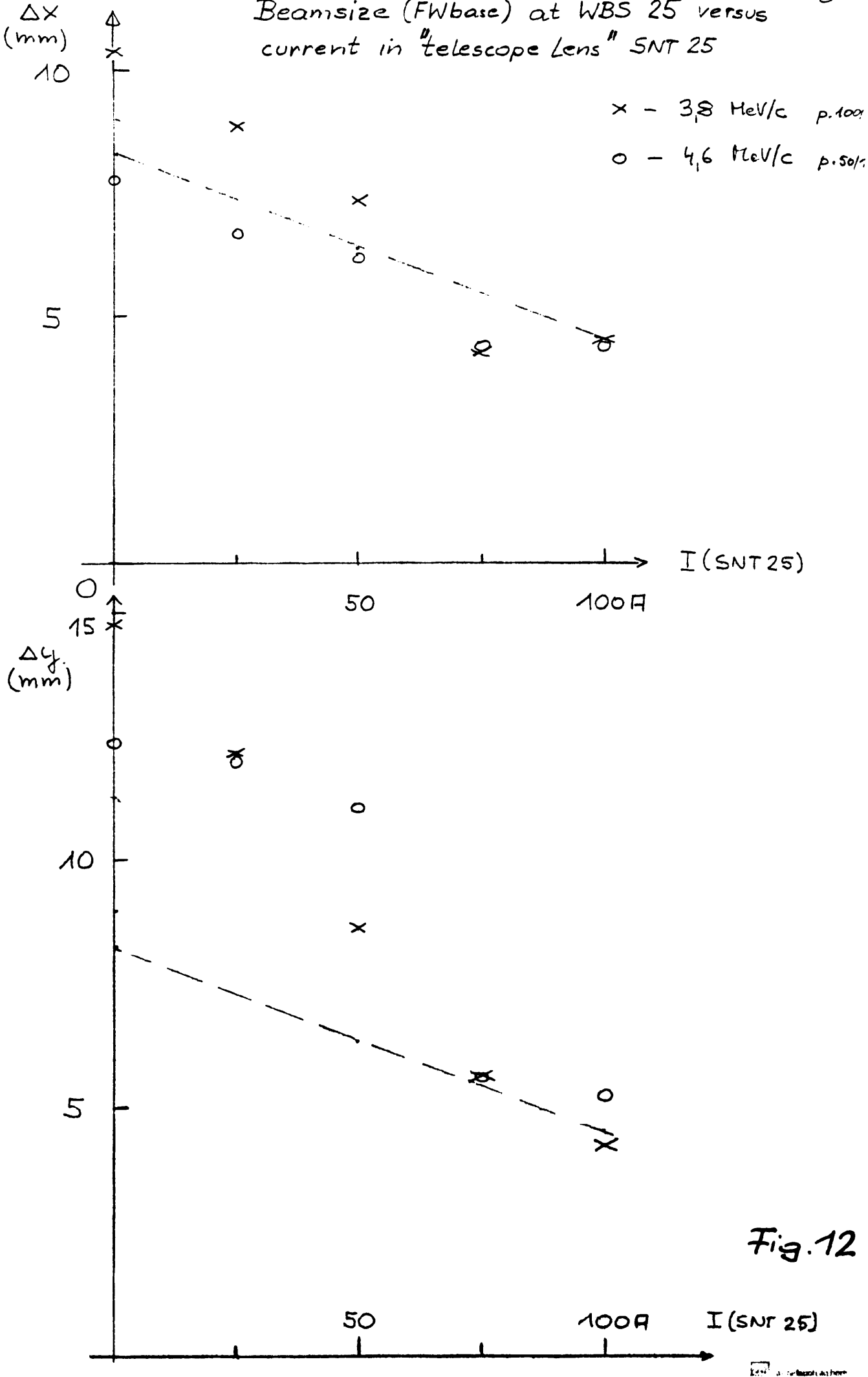

Fig. 12

Fig. 12

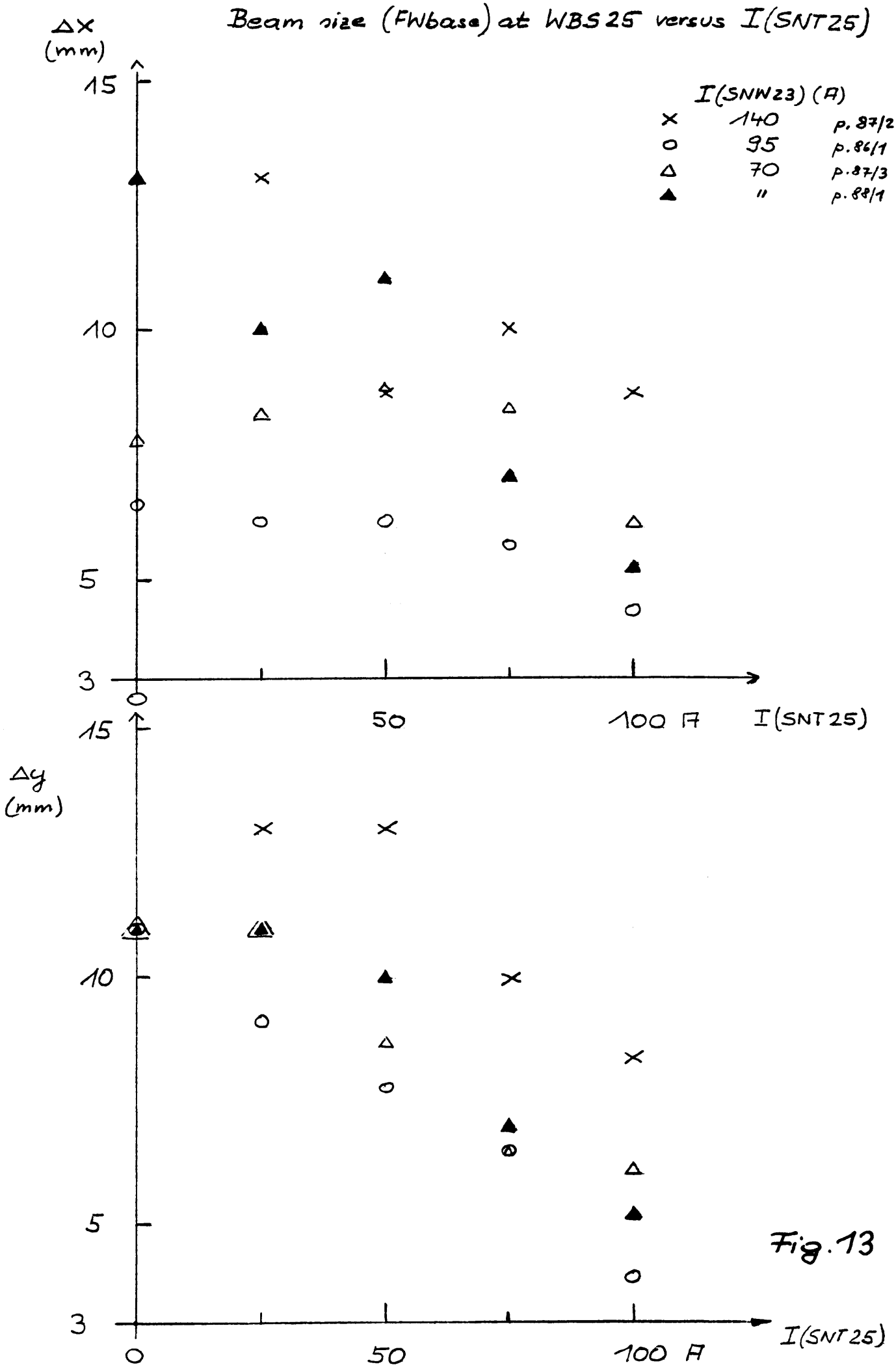
Beam size (FWbase) at WBS25 versus I(SNT25)
ΔX (mm)
15
10
5
3
I(SNW23) (A)
140 p. 87/2
95 p. 86/1
70 p. 87/3
" p. 88/1
0
50
100 A
I(SNT25)
Δy (mm)
15
10
5
3
0
50
100 A
I(SNT25)

Fig. 13

Beam current after 5mm Ø diaphragma versus I(SNT25)

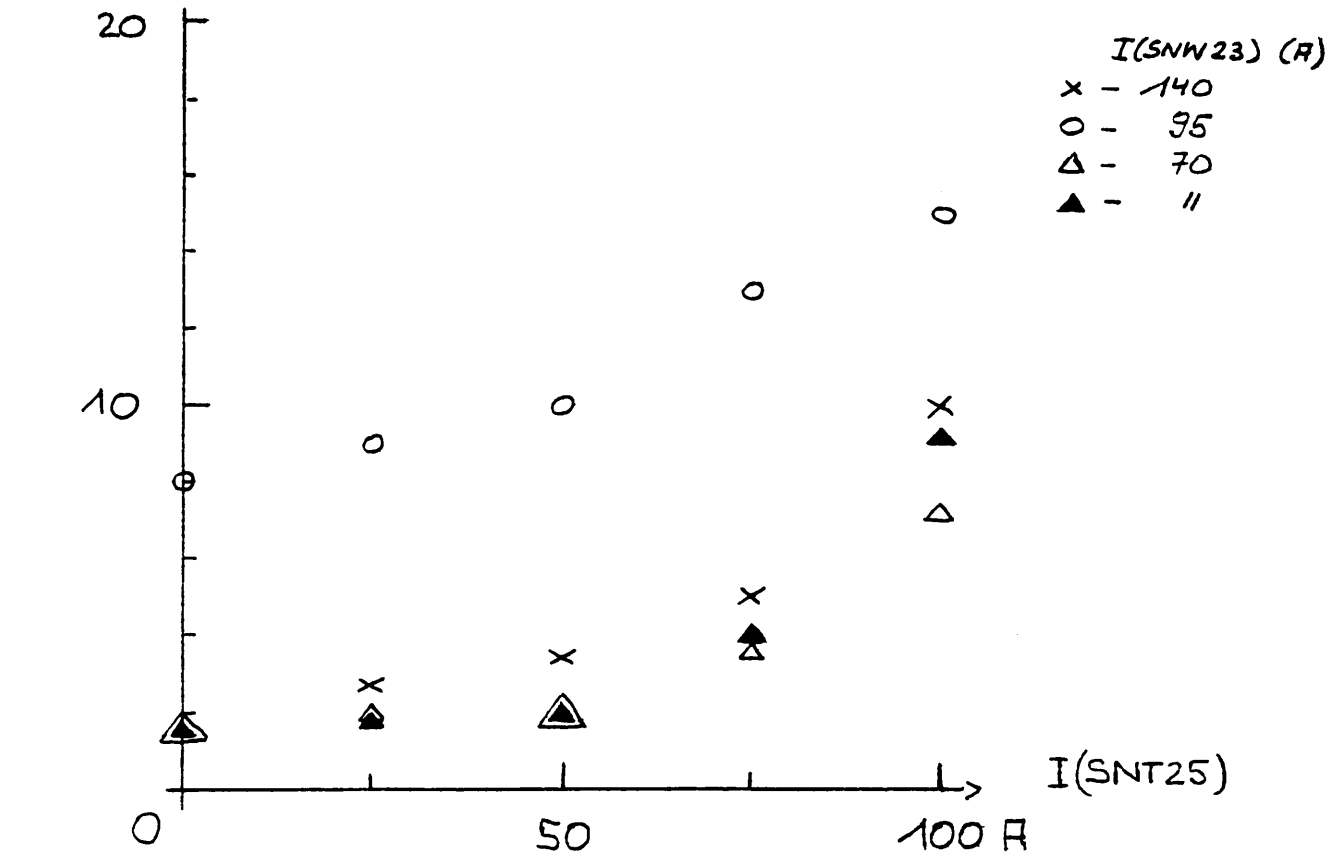

Fig. 13 4

Fig. 14

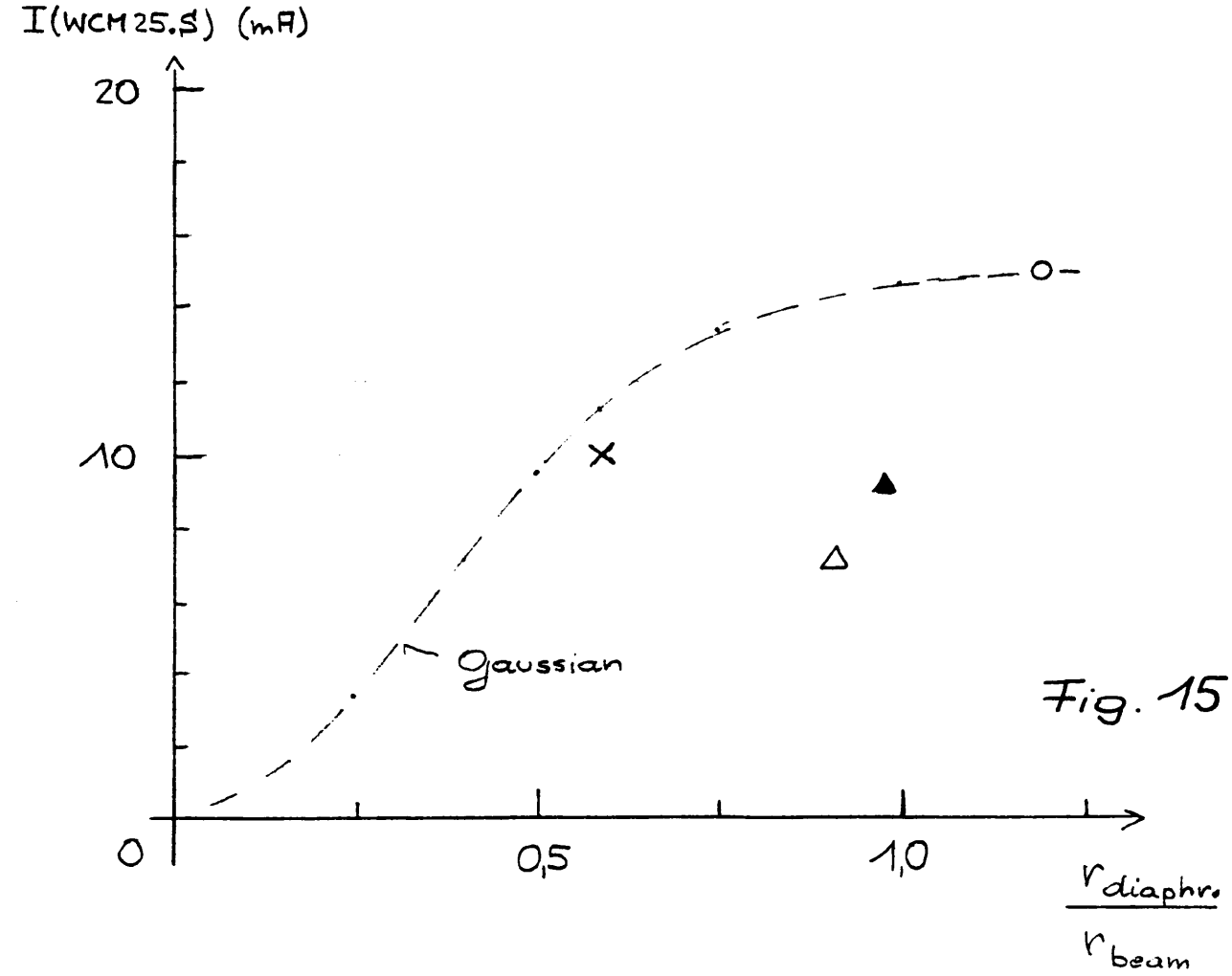

Fig. 15

Fig. 14 5

Projection of 5mm ϕ diaphragma back to exit buncher

Parameter : SNT 25 current

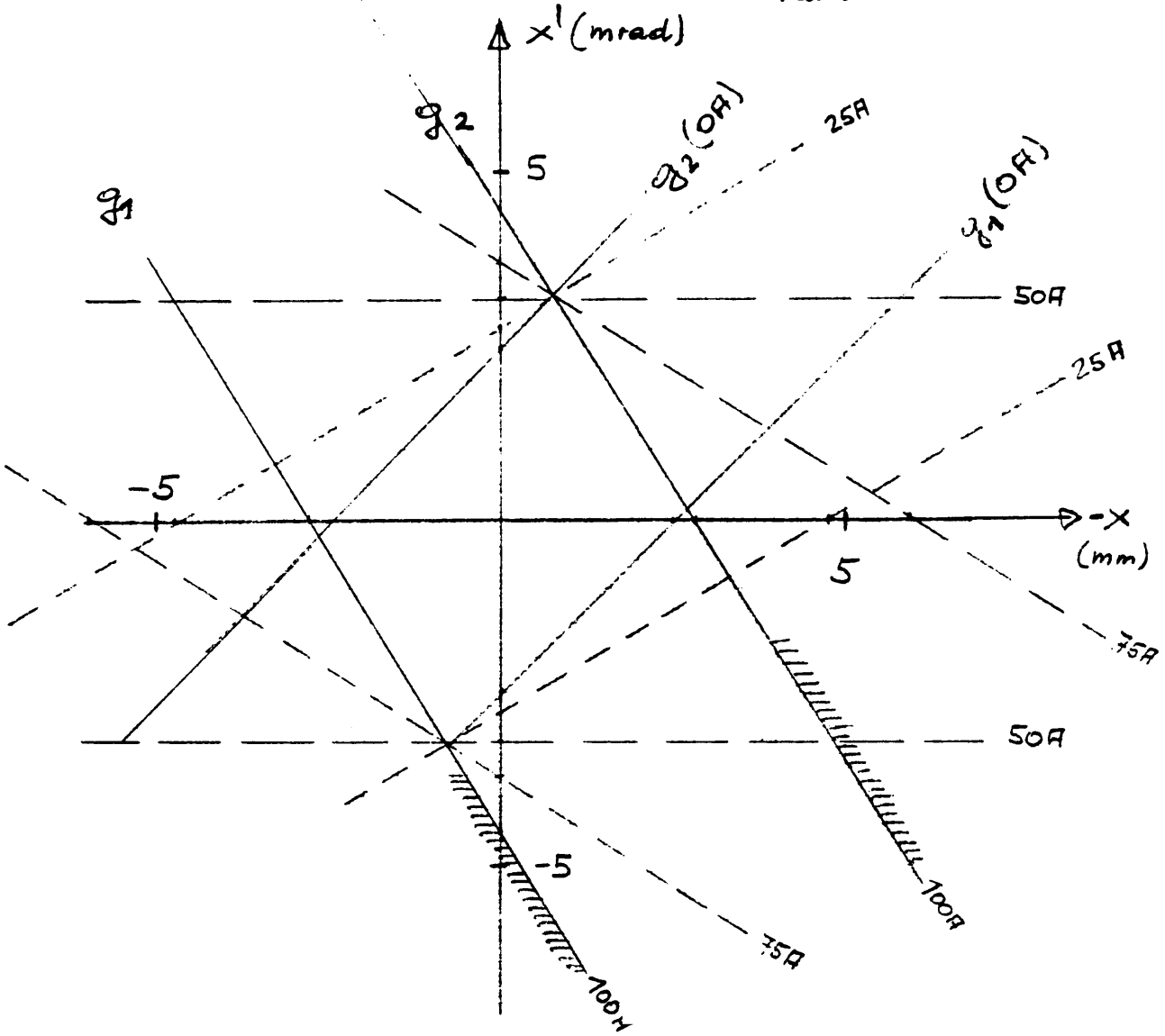

Limitation in phase space at diaphragma 5mm ϕ

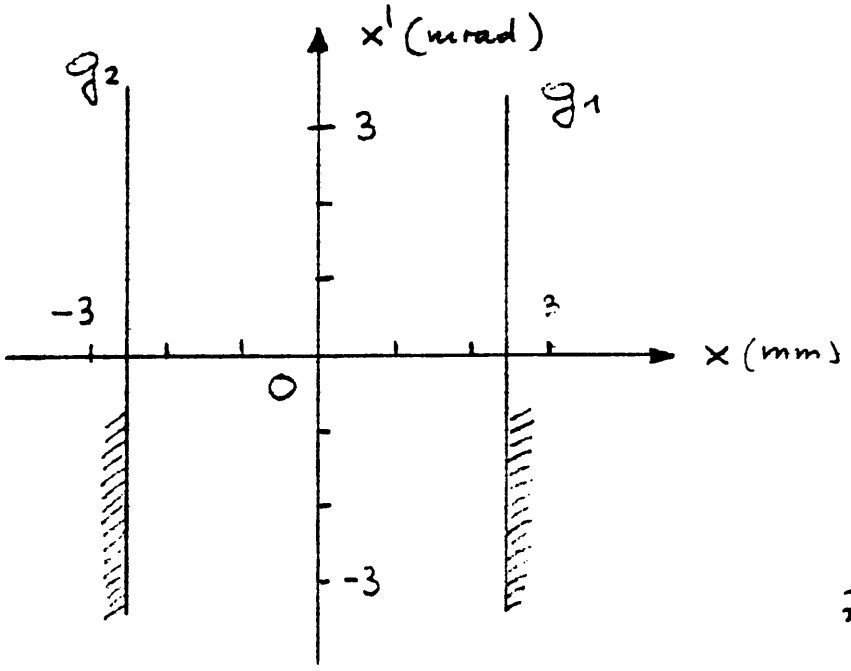

Fig. 16

Fig 16/15

Fig. 16

DISTRIBUTION

Authors

- LAL R. Belbeoch
  R. Chaput
  R. Chehab
  F. Dupont
  J. Le Duff

- CERN J.P. Delahaye/PS
  B. Frammery/PS
  W. Heinze/PS
  B. Kuiper/PS
  J.P. Potier/PS
  B. Szeless/PS